

# Corrosion Inhibition and Adsorption Properties of *N*-{2-[2-(5-Methyl-1*H*-pyrazol-3-yl)acetamido]phenyl}benzamide Monohydrate on C38 Steel in 1 M HCl: Insights from Electrochemical Analysis, DFT, and MD Simulations

Karim Azgaou, Rachid Hsissou, Karim Chkirate, Mohammed Benmessaoud, Mohamed Hefnawy, Ali El Gamal, Hicham Elmsellem, Lei Guo, El Mokhtar Essassi, Souad El Hajjaji, and Nada Kheira Sebbar\*



Cite This: *ACS Omega* 2025, 10, 6244–6257



Read Online

ACCESS |



Metrics & More

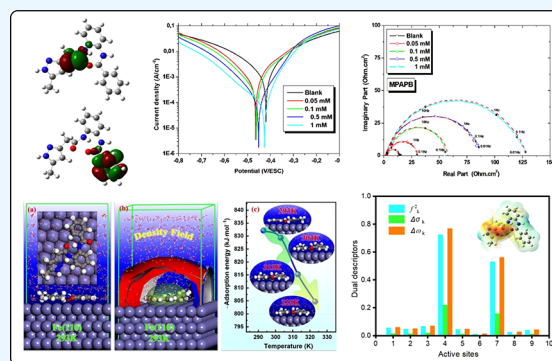


Article Recommendations



Supporting Information

**ABSTRACT:** The heterocyclic compound *N*-{2-[2-(5-methyl-1*H*-pyrazol-3-yl)acetamido]-phenyl}benzamide monohydrate (MPAPB) was synthesized and structurally characterized by using nuclear magnetic resonance (NMR), mass spectrometry, and infrared (IR) spectroscopy. Its corrosion inhibition performance for C38 in 1 M HCl was evaluated by using gravimetric weight loss measurements, electrochemical impedance spectroscopy (EIS), and potentiodynamic polarization (PDP) techniques. MPAPB demonstrated a high inhibition efficiency of 90.2% at a concentration of 1 mM, accompanied by a substantial decrease in the corrosion current density. Electrochemical results revealed that MPAPB acts as a mixed-type inhibitor, reducing both anodic and cathodic reactions, while increasing the charge transfer resistance ( $R_p$ ) and decreasing the double-layer capacitance ( $C_{dl}$ ), indicative of effective surface adsorption. The adsorption behavior of MPAPB was consistent with that of the Langmuir adsorption isotherm, suggesting a combination of physical and chemical adsorption mechanisms. Density functional theory (DFT) calculations and molecular dynamics (MD) simulations further elucidated the interaction between the MPAPB and the steel surface, highlighting the role of electron-donating heteroatoms and  $\pi$ -electron systems in adsorption. These theoretical findings were in agreement with the experimental results, confirming the formation of a protective layer that inhibits corrosion.



## 1. INTRODUCTION

Corrosion is continuously significant across several industries, especially when metallic surfaces are subjected to harsh conditions, such as in the petrochemical, maritime, and construction sectors.<sup>1</sup> In acidic environments, such as hydrochloric acid (HCl), often used in industrial cleaning and pickling, metals such as mild steel (C38) exhibit significant susceptibility to corrosion. The deterioration of metals from corrosion may result in substantial economic losses and operational breakdowns. Consequently, finding effective methods to protect metals from corrosive attacks is essential in materials research and industrial applications. Several methods are employed to protect steel surfaces, such as corrosion inhibition,<sup>2,3</sup> coatings and paints,<sup>4,5</sup> and thin films.

Among these, corrosion inhibitors, especially organic compounds, are widely employed because they are cost-effective and easy to apply and provide robust protection.<sup>6–9</sup> Organic corrosion inhibitors work primarily by adsorbing onto the metal surface, forming a protective barrier that blocks the interaction between the corrosive medium and the metal. This

adsorption depends on the chemical structure of the inhibitor, the presence of heteroatoms with lone pairs of electrons, and conjugated  $\pi$ -electron systems.<sup>10–14</sup>

Heterocyclic compounds are recognized for their versatility due to their molecular structure, which contains heteroatoms (such as nitrogen, oxygen, sulfur, and phosphorus) and unsaturated aromatic rings. These structural features provide multiple adsorption sites, allowing the compounds to interact strongly with the metal surfaces. The heteroatoms, with their lone pairs of electrons, act as electron donors, facilitating the formation of coordination bonds with the vacant d-orbitals of the metal atoms. Meanwhile, the  $\pi$ -electrons in the unsaturated

**Received:** December 24, 2024

**Revised:** January 12, 2025

**Accepted:** January 20, 2025

**Published:** February 3, 2025



aromatic rings contribute to the adsorption process by forming additional interactions with the metal surface.<sup>15–17</sup> The effectiveness of heterocyclic compounds relies on factors such as the electron density surrounding the heteroatoms, the quantity of adsorption-active centers in the molecule, the size of the molecule, the mode of adsorption, and the formation of metallic complexes.<sup>18</sup>

Pyrazole and its derivatives encompass various organic compounds used in industrial and biological applications.<sup>19</sup> These compounds are of significant interest in industrial and biological applications due to their diverse chemical, pharmacological, and industrial properties. Over the years, pyrazole derivatives have been extensively studied and utilized in various fields, ranging from pharmaceuticals to corrosion science. In pharmaceutical research, pyrazole derivatives have been frequently explored for their therapeutic potential. A growing body of literature has demonstrated that many of these compounds exhibit notable anti-inflammatory, antimicrobial, anticancer, and analgesic properties, making them promising candidates for treating various diseases and disorders.<sup>20,21</sup> The anticancer properties of pyrazole derivatives have also been well-documented, with certain compounds demonstrating the ability to inhibit the proliferation of cancer cells and prevent metastasis.<sup>22,23</sup>

The growing demand for pyrazole derivatives has driven synthetic chemistry researchers to explore their applications beyond the pharmaceutical field, where they are well-known for their biological activities. Notably, pyrazole derivatives have shown significant promise as corrosion inhibitors for various metals in acidic environments. Their high efficiency is often attributed to their heterocyclic structure, which allows for strong adsorption onto metal surfaces, forming protective films that reduce the corrosion rates. Numerous studies have reported on the corrosion inhibition performance of different pyrazole-based compounds. Table 1 presents a summary of the inhibition efficiencies of selected pyrazole derivatives for steel in an acidic medium.<sup>24–32</sup>

In this context, the current study introduces a novel pyrazole derivative, *N*-{2-[2-(5-methyl-1*H*-pyrazol-3-yl)acetamido]-phenyl}benzamide monohydrate (MPAPB), as a potential corrosion inhibitor for C38 steel in 1 M HCl. The compound demonstrates a high inhibition efficiency of 90% at 10<sup>−3</sup> M, comparable to or exceeding those reported for similar compounds in the literature.

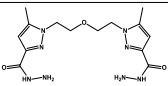
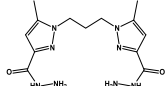
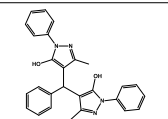
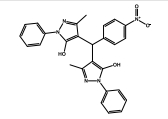
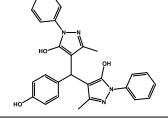
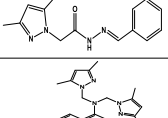
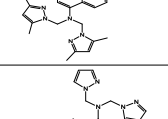
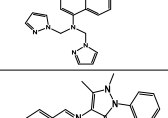
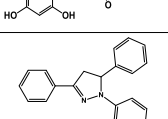
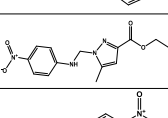
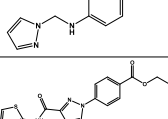
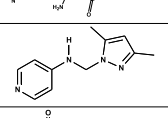
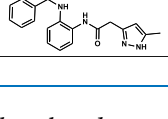
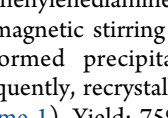
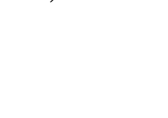
The present study aims to evaluate a newly synthesized heterocyclic compound as a corrosion inhibitor for C38 steel in a 1 M HCl medium. To assess its efficacy, weight loss measurements, polarization curves (PC), and electrochemical impedance spectroscopy (EIS) will be employed. Additionally, the influence of temperature on the corrosion behavior will be studied over a range of 293 to 323 K. Quantum chemical descriptors (QCDs) will be calculated using density functional theory (DFT) at the B3LYP level with the 6-31G(d,p) basis set. To further investigate the interaction and inhibition mechanism of the synthesized compound with the iron surface, molecular dynamics (MD) simulations will also be conducted.

## 2. EXPERIMENTAL PROCEDURE

### 2.1. Synthesis of Compounds (3), (4), and (MPAPB).

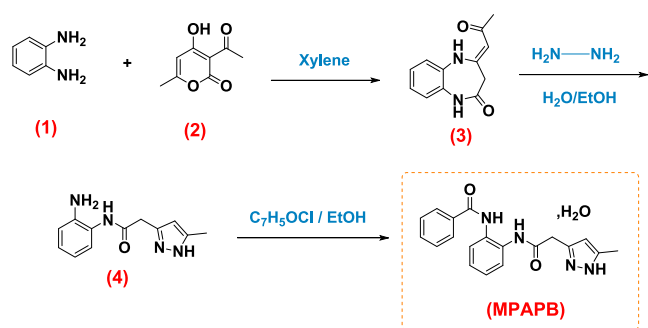
**2.1.1. Preparation of 4*Z*-(2-Oxopropylidene)-1,5-benzodiazepin-2-one (3).** 1,5-Benzodiazepin-2-one (3) was synthesized using a procedure reported in the literature.<sup>33,34</sup> A blend of 0.02 mol (3.36 g) of dehydroacetic acid and 0.04 mol (4.32 g)

**Table 1. Extracted Results Obtained on Corrosion Inhibition Behavior of Different Pyrazole Compounds in Different Media**

| Inhibitors   | Concentration | Metal        | Medium                              | IE%  | Ref.      |
|--|---------------|--------------|-------------------------------------|------|-----------|
|    | 1 mM          | mild steel   | 1M HCl                              | 77   | [22]      |
|    | 1 mM          | mild steel   | 1M HCl                              | 91   | [22]      |
|    | 0.366 mM      | mild steel   | 1M HCl                              | 84   | [23]      |
|    | 0.366 mM      | mild steel   | 1M HCl                              | 86   | [23]      |
|    | 0.366 mM      | mild steel   | 1M HCl                              | 86   | [23]      |
|    | 1 mM          | mild steel   | 1M HCl                              | 75.7 | [24]      |
|   | 1 mM          | Mild steel   | 0.5M H <sub>2</sub> SO <sub>4</sub> | 89   | [25]      |
|  | 1 mM          | Mild steel   | 0.5M H <sub>2</sub> SO <sub>4</sub> | 91   | [25]      |
|  | 0.1 mM        | carbon steel | 1M HCl                              | 87   | [26]      |
|  | 1 mM          | carbon steel | 1M HCl                              | 90   | [27]      |
|  | 1 mM          | carbon steel | 1M HCl                              | 89.  | [28]      |
|  | 1 mM          | carbon steel | 1M HCl                              | 88   | [28]      |
|  | 1 mM          | carbon steel | 1M HCl                              | 83   | [29]      |
|  | 1 mM          | mild steel   | 1M HCl                              | 88   | [30]      |
|  | 1 mM          | carbon steel | 1M HCl                              | 90   | This work |

of *o*-phenylenediamine in xylene (80 mL) underwent heating with magnetic stirring for 4 h. Following the cooling process, the formed precipitate was subjected to filtration, and subsequently, recrystallization was carried out utilizing ethanol (Scheme 1). Yield: 75%; M.P. (K): 511; <sup>1</sup>H NMR (300 MHz,

### Scheme 1. Synthetic Pathway for the Preparation of the Studied Compound (MPAPB)



DMSO- $d_6$ ,  $\delta$ (ppm): 2.00 (s, 3H,  $\text{CH}_3$ ); 3.00 (s, 2H,  $\text{CH}_2$ ); 5.20 (s, 1H, aliphatic CH); 7.10 (m, 4H, aromatic CH); 8.83 (s, 1H, NH amide) and 9.96 (s, 1H, NH amine); FTIR (ATR,  $\gamma(\text{cm}^{-1})$ ): 3321–3207 (band NH amine and amide); 1671 ( $\text{C}=\text{O}$  cyclic), 1607 (band  $\text{C}=\text{O}$  acyclic), and 1575 (band  $\text{C}=\text{C}$ ); MS: (ESI);  $m/z = 217[\text{MH}]^+$ .

**2.1.2. Synthesis of *N*-(2-Aminophenyl)-2-(5-methyl-1H-pyrazol-3-yl)acetamide (4).** A blend of 2 g of 4Z-(2-oxopropylidene)-1,5-benzodiazepin-2-one and the stoichiometric amount of hydrazine hydrate was heated to reflux for 2 h in 40 mL of ethanol (solvent). Once the solvent volume had been concentrated to 20 mL, the mixture was kept at rest; the precipitate obtained was filtered and then recrystallized from ethanol. Yield: 80%; M.P. (K): 445;  $^1\text{H}$  NMR (300 MHz, DMSO- $d_6$ ,  $\delta$ (ppm)): 2.51 (s, 3H,  $\text{CH}_3$ ), 2.20 (s, 2H,  $\text{CH}_2$ ), 4.86 (s, 2H,  $\text{NH}_2$ ), 5.94 (s, 1H, H pyrazole), 6.52–7.16 (m, 4H, H aromatic), 9.25 (s, 1H, NH amide), 12.24 (s, 1H, NH pyrazole); FTIR (ATR,  $\gamma(\text{cm}^{-1})$ ): 3000–3400 (NH,  $\text{NH}_2$ ), 1737 ( $\text{C}=\text{O}$ ); 1655 ( $\text{C}=\text{N}$ ); MS (ESI):  $m/z = 230[\text{MH}]^+$ .

**2.1.3. Synthesis of *N*-[2-[2-(5-Methyl-1H-pyrazol-3-yl)-acetamide]-phenyl]benzamide Monohydrate (MPAPB).** To a solution of 5.10–4 mol of *N*-(2-aminophenyl)-5-methyl-1H-pyrazol-3-yl)acetamide in 10 mL of ethanol was added to 5.10–4 mol of benzoyl chloride under magnetic stirring at room temperature for 4 h. After filtration and recrystallization from ethanol, colorless single crystals were produced in 66% yield (Scheme 1). M.P (K): 502–504;  $^1\text{H}$  NMR (300 MHz, DMSO- $d_6$ ,  $\delta$ (ppm)): 2.21 (s, 3H,  $\text{CH}_3$ ), 3.89 (s, 2H,  $\text{CH}_2$ ), 6.31 (s, 1H, CH pyrazole), 7.23–7.98 (m, 9H, CH aromatic), 8.00 (s, 1H, NH  $\text{CH}_2$ –CO (amide)), 9.94 (s, 1H, NH Ar–CO (amide)), and 10.25 (s, 1H, NH pyrazole).  $^{13}\text{C}$  NMR (75 MHz, DMSO- $d_6$ ,  $\delta$ (ppm)): 11.09 ( $\text{CH}_3$ ), 34.16 ( $\text{CH}_2$ ), 106.43 (C pyrazole), 125.36–131.12 and 131.43–134.62 (C aromatic), 143.33 and 144.01 (C pyrazole), 165.62 and 167.30 ( $\text{C}=\text{O}$ ); FTIR (ATR,  $\gamma(\text{cm}^{-1})$ ): 3225.56 (NH), 1674.76 and 1646.75 ( $\text{C}=\text{O}$ ); MS (ESI):  $m/z = 335.15[\text{MH}]^+$  (see Figures S1 and S4).

**2.2. Used Material and Solution.** The synthesized compound (MPAPB) was applied at various concentrations (from 0.05 to 1 mM) for C38 steel in a 1 M HCl medium. The C38 steel, measuring 1 cm  $\times$  1 cm, is characterized by the following weight percentages of its elemental composition: 0.370% carbon (MPAPB), 0.230% silicon (Si), 0.680% manganese (Mn), 0.016% sulfur (S), 0.077% chromium (Cr), 0.011% titanium (Ti), 0.059% nickel (Ni), 0.009% cobalt (Co), 0.160% copper (Cu), with the remaining balance being iron (Fe). In addition, a corrosive solution of 1 M HCl

was prepared by diluting analytical acid (37% HCl) with distilled water at room temperature.

**2.3. Electrochemical Characterization.** The electrochemical investigation was conducted using a potentiostat PGZ101 Volta Master apparatus. In the electrochemical test, we used three-electrode cells composed of C38 steel as the working electrode, platinum (Pt) as the counter electrode, and a saturated calomel electrode (SCE) as the reference electrode, respectively. Before conducting all experiments, the potential was allowed to stabilize at the free potential for 30 min. Furthermore, potentiodynamic polarization analysis was conducted at a scan rate of 1 mV/s from  $-800$  to  $-0.1$  mV. Subsequently, electrochemical curves were performed with open circuit potential in the frequency range of 100 kHz to 10 mHz with a signal amplitude of 10 mV.

**2.4. SEM Analysis.** The C38 steel surface was examined by using SEM analysis without and in the presence of the MPAPB compound. SEM images were obtained using a Quattro ESEM-FEG instrument at a 20 kV accelerating voltage and a magnification of  $\times 4000$ .

**2.5. Computational Details.** The DFT method was utilized to analyze the reactivity of the compound and compare it to the experimental results. Global quantum chemical descriptors (GQCDs), including the energy of the highest occupied molecular orbital ( $E_{\text{HOMO}}$ ), energy of the lowest unoccupied molecular orbital ( $E_{\text{LUMO}}$ ), electron affinity (EA), ionization energy (IE), energy gap ( $\Delta E_{\text{gap}}$ ), electronegativity ( $\chi$ ), softness ( $\sigma$ ), hardness ( $\eta$ ), nucleophilicity ( $\epsilon$ ), electrophilicity ( $\omega$ ), and electrons transferred from the inhibitor to metal ( $\Delta N_{110}$ ), were calculated using eqs 1–9.<sup>35</sup> Recently, the geometry and electronic structure of the investigated inhibitor were carried out using the DFT method at B3LYP with the 6-31G(d,p) basis set.<sup>36–38</sup> The computations were performed employing the Gaussian 09 software package.<sup>39</sup>

$$\text{IE} = -E_{\text{HOMO}} \quad (1)$$

$$\text{EA} = -E_{\text{LUMO}} \quad (2)$$

$$\Delta E_{\text{gap}} = E_{\text{LUMO}} - E_{\text{HOMO}} \quad (3)$$

$$\chi = \frac{I + A}{2} \quad (4)$$

$$\eta = \frac{\Delta E_{\text{gap}}}{2} \quad (5)$$

$$\sigma = \frac{1}{\eta} \quad (6)$$

$$\omega = \frac{\chi^2}{2\eta} \quad (7)$$

$$\epsilon = \frac{1}{\omega} \quad (8)$$

$$\Delta N_{110} = \frac{\Phi_{\text{Fe}(110)} - \chi_{\text{inh}}}{2(\eta_{\text{Fe}} + \eta_{\text{inh}})} \quad (9)$$

where  $\Phi_{\text{Fe}(110)}$ ,  $\chi_{\text{inh}}$ ,  $\eta_{\text{Fe}}$ , and  $\eta_{\text{inh}}$  are the work function of Fe(110) (5.07 eV), the electronegativity of the inhibitor studied, the absolute hardness of iron (0.0 eV), and the hardness of the studied molecule, respectively. Further, molecular dynamics (MD) simulation calculations were carried

out according to the procedure reported in many studies in the literature.<sup>35,40,41</sup>

### 3. RESULTS AND DISCUSSION

**3.1. Weight Loss Measurements.** Weight loss experiments were conducted to assess the inhibition effectiveness of the newly synthesized inhibitor (MPAPB) at various concentrations for C38 steel after 24 h of immersion in a 1 M HCl solution at 293 K. Further, the corrosion rate and the inhibition efficiency values are summarized in Table 2. Also, the corrosion rate ( $W_{\text{corr}}$ ) and inhibition efficiency (IE %) are computed according to eqs 10 and 11,<sup>11,42,43</sup>

$$W_{\text{corr}} = \frac{\Delta m}{S \times t} \quad (10)$$

$$\text{IE}(\%) = \frac{W_{\text{corr}} - W_{\text{corr}}^{\text{inh}}}{W_{\text{corr}}} \times 100 \quad (11)$$

**Table 2. Corrosion Parameters Derived from Weight Loss Experiments for C38 Steel in 1M HCl with Different Concentrations of (MPAPB) at 293 K**

| concentration (mM) | $W_{\text{corr}}$ (mg cm <sup>-2</sup> h <sup>-1</sup> ) | IE (%) |
|--------------------|--|--------|
| blank              | 0.53   | —      |
| 0.05               | 0.27   | 48.0   |
| 0.1                | 0.10   | 79.6   |
| 0.5                | 0.07   | 86.5   |
| 1.0                | 0.02   | 95.1   |

Let  $\Delta m$ ,  $S$ , and  $t$  represent the mass variation between the C38 steel substrate before and after corrosion, the surface area of C38 steel, and the immersion time, respectively. Additionally,  $W_{\text{corr}}$  and  $W_{\text{corr}}^{\text{inh}}$  are the weight loss without and with the tested inhibitor at varying concentrations, respectively.

As per the information provided in Table 2, it is apparent that the corrosion rate gradually declines as the concentration of the tested inhibitor (MPAPB) increases. This observation implies that the introduction of the inhibitor effectively retards the corrosion of the C38 steel. Moreover, the inhibitory efficiency shows an ascending trend with rising concentrations, reaching its peak at 95.1% with an optimal concentration of 1.0 mM of (MPAPB) after 24 h of immersion.<sup>44,45</sup> This trend is attributed to the robust adsorption of the inhibitor (MPAPB) onto the metal surface.<sup>46–48</sup> Consequently, the results suggest that an elevated inhibitor concentration produces more adsorbed inhibitor molecules on the C38 steel surface. This, in turn, leads to blocking more corrosion-active sites, thereby enhancing the prevention of weight loss more effectively.

**3.2. Polarization Plots.** Figure 1 illustrates the polarization plots for C38 steel in a 1 M HCl solution for both uninhibited and inhibited media after the addition of various concentrations of the tested inhibitor (MPAPB). In addition, various electrochemical parameters are outlined in Table 3. The corrosion inhibition efficiency (IE%) was computed using the equation provided in eq 12:<sup>46,49</sup>

$$\text{IE}(\%) = \frac{i_{\text{corr}} - i_{\text{corr}}^{\text{inh}}}{i_{\text{corr}}} \times 100 \quad (12)$$

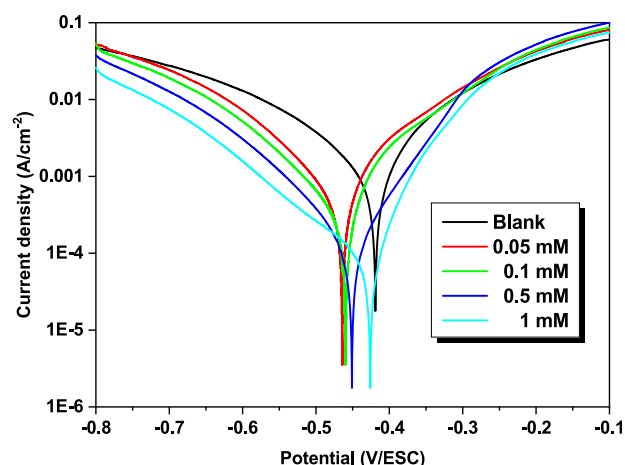


**Figure 1.** Polarization plots of C38 steel in 1 M HCl before and after adding different concentrations of the inhibitor tested (MPAPB) at 303 K.

**Table 3. Electrochemical Properties with the Corresponding Inhibition Efficiencies Were Measured for C38 Steel before and after the Addition of the Test Compound (MPAPB) to 1 M HCl**

| C [mM]  | $-E_{\text{corr}}$ (mV/SCE) | $i_{\text{corr}}$ ( $\mu\text{A cm}^{-2}$ ) | $\beta_a$ (mV dec <sup>-1</sup> ) | $-\beta_c$ (mV dec <sup>-1</sup> ) | IE (%) |
|---------|-----------------------------|---|-----------------------------------|------------------------------------|--------|
| 1 M HCl | 419                         | 879.6                                       | 92.5                              | 148.0                              | —      |
| 0.05    | 465                         | 490.0                                       | 78.1                              | 110.9                              | 44.3   |
| 0.1     | 460                         | 311.1                                       | 63.9                              | 110.8                              | 64.6   |
| 0.5     | 451                         | 140.5                                       | 75.5                              | 106.5                              | 84.0   |
| 1.0     | 426                         | 77.6  | 60.0                              | 139.8                              | 91.2   |

here  $i_{\text{corr}}$  and  $i_{\text{corr}}^{\text{inh}}$  denote the uninhibited corrosion current density and the inhibited corrosion current density, respectively.

The examination of Figure 1 indicates that the addition of various concentrations of the inhibitor (MPAPB) inhibits both cathodic and anodic segments of the polarization plots, resulting in displacements toward smaller current densities. This can be ascribed to the adsorption of this organic compound on the C38 surface. Consequently, Inhibitor C can be classified as a mixed-type inhibitor. This observation suggests that adding 1 mM does not affect the cathodic reaction and that hydrogen reduction on the C38 surface occurs principally via a charge-transfer mechanism. The reduction observed in the cathodic segment may be due to the adsorption of the compound (MPAPB) on the cathodic sites.

Consequently, introducing this inhibitor (MPAPB) not only diminishes the dissolution of C38 steel but also delays hydrogen evolution reactions. On the anodic branch of the polarization curve, the inhibitors are initially adsorbed on the C38 surface, thus blocking the available active sites.<sup>50</sup> Surface coverage shows an upward trend with increasing inhibitor concentrations. The development of a thin barrier layer covering the C38 steel surface limits the number of active sites that can be attacked by corrosion. This film effectively retards the evolution of hydrogen, and metal dissolution provides substantial corrosion protection for C38 steel.<sup>51</sup> The electrochemical parameters extracted from these plots are outlined in Table 3. The corrosion current density ( $i_{\text{corr}}$ ) values



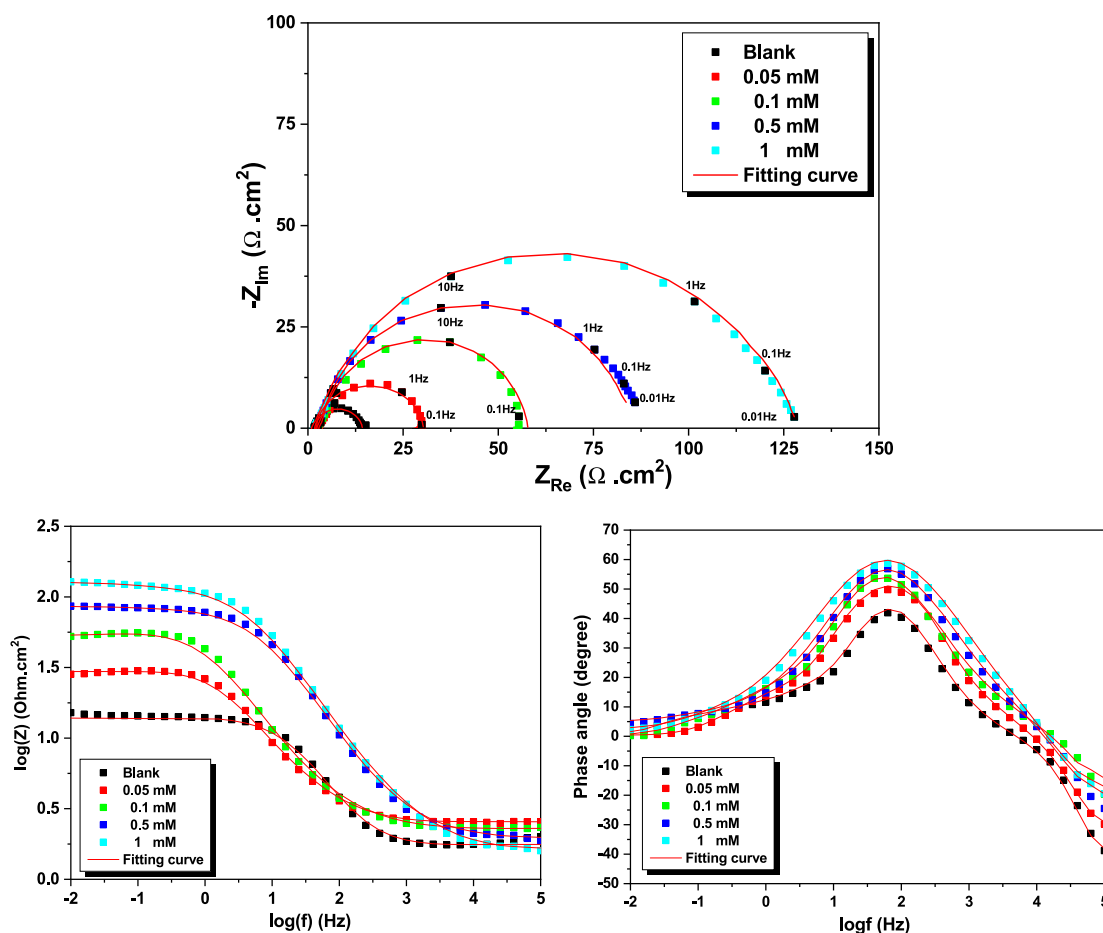


**Figure 2.** Nyquist, Bode, and phase angle diagrams of C38 steel in 1 M HCl without and with various concentrations of the tested inhibitor.

significantly decrease with escalating concentrations of the tested inhibitor (MPAPB). This reduction is attributed to the development of a barrier layer covering the C38 steel surface. Simultaneously, the inhibition effectiveness rises as inhibitor concentrations rise, reaching a maximum of 91.2% at the optimum concentration of 1.0 mM.

**3.3. EIS Measurements.** Figure 2 shows Nyquist plots, Bode plots, and phase angle plots for C38 steel under uninhibited (Blank) and inhibited conditions with varying concentrations of the synthesized inhibitor (MPAPB). The capacitive curves shown in the Nyquist diagrams are not centered on the real axis, suggesting frequency dispersion associated with surface heterogeneity. This dispersion is linked to factors including impurities, surface rugosity, delocalization, adsorption of the compound, and the formation of porous layers.<sup>52,53</sup> As depicted in Figure 2, the diameter of the capacitive loops after adding the synthesized inhibitor is higher than that for the blank solution. This observation indicates that the corrosion phenomena of C38 steel in a 1 M HCl solution are prevented due to the inhibitive properties of the inhibitor on the metal surface.<sup>54</sup>

The capacitive loop represents the charge transfer resistance ( $R_{ct}$ ), diffuse layer resistance ( $R_{dl}$ ), and resistance from other accumulations at the metal/solution interface ( $R_a$ ), which collectively contribute to the polarization resistance ( $R_p = R_{ct} + R_{dl} + R_a$ ). The deviation of the capacitive loop from an ideal capacitor is commonly explained by frequency dispersion, which occurs due to the inhomogeneity of the metal surface.<sup>55,56</sup> Different electrochemical impedance spectroscopy

parameters, such as the solution resistance ( $R_s$ ), the charge transfer resistance ( $R_p$ ), double layer capacitance ( $C_{dl}$ ), and inhibition efficiency (IE%), are shown in Table 4. The

**Table 4.** EIS Parameters for C38 Steel in a 1M HCl Solution, Both in the Absence and Presence of Various Concentrations of the Studied Inhibitor (MPAPB) at 293 K

| C (mM) | $R_s$ ( $\Omega \cdot \text{cm}^2$ ) | $R_p$ ( $\Omega \cdot \text{cm}^2$ ) | $C_{dl}$ ( $\mu\text{F} \cdot \text{cm}^{-2}$ ) | IE (%) | $\theta$ |
|--------|--------------------------------------|--------------------------------------|---|--------|----------|
| 0      | $2.7 \pm 0.2$                        | $12.5 \pm 0.5$                       | $804.0 \pm 2.5$                                 | —      |          |
| 0.05   | $2.8 \pm 0.2$                        | $28.2 \pm 0.8$                       | $564.0 \pm 1.8$                                 | 55.6   | 0.556    |
| 0.1    | $2.8 \pm 0.3$                        | $55.4 \pm 0.7$                       | $453.9 \pm 1.5$                                 | 77.4   | 0.774    |
| 0.5    | $3.0 \pm 0.4$                        | $82.2 \pm 1.1$                       | $484.1 \pm 1.5$                                 | 84.8   | 0.848    |
| 1      | $2.9 \pm 0.4$                        | $127.7 \pm 2.4$                      | $311.4 \pm 1.2$                                 | 90.2   | 0.902    |

inhibition efficiency (%) for C38 steel derived from these EIS graphs was then obtained by applying eq 13:

$$\text{IE}(\%) = \frac{R_{ct}^{\text{inh}} - R_{ct}^0}{R_{ct}^{\text{inh}}} \times 100 \quad (13)$$

where  $R_{ct}^0$  and  $R_{ct}^{\text{inh}}$  denote the charge transfer resistance without and in the presence of varying concentrations of the inhibitor tested (MPAPB), respectively.

The Nyquist plots presented in Figure 2 reveal a single capacitive loop, which signifies that the corrosion process of C38 steel in a 1 M HCl solution is predominantly governed by a charge transfer mechanism.<sup>57</sup> This observation is consistent with findings in the literature, which suggest that the corrosion

of steel in acidic media is primarily controlled by electron transfer at the metal/solution interface, rather than by other processes such as mass transport or diffusion. The existence of a single loop, confirmed in both the Nyquist and Bode plots, suggests that the corrosion mechanism remains unchanged with the addition of the inhibitor, reinforcing the idea that the inhibitor does not alter the fundamental corrosion process. Instead, it operates primarily through surface adsorption, acting as a protective barrier on the steel surface, thereby reducing the rate of corrosion without disrupting the electrochemical pathways that lead to steel dissolution.<sup>58–60</sup> On the other hand, capacitive loop diameters increase with higher inhibitor concentrations. This phenomenon is ascribed to the formation of a thin barrier layer over the steel surface, which helps improve inhibition performance. As indicated in Table 4, inhibition efficacy clearly rises with higher concentrations of the inhibitor tested (MPAPB). It achieves its maximum value of 90.2% at the optimum concentration of 1 mM, corresponding to a higher value of  $R_p$  ( $127.7 \Omega \text{ cm}^2$ ). The double-layer capacitance ( $C_{dl}$ ) decreases in parallel with that of the pure 1 M HCl solution (blank solution). Simultaneously, the double-layer capacitance ( $C_{dl}$ ) decreases from  $804 \mu\text{F}\cdot\text{cm}^{-2}$  (in the absence of the inhibitor) to  $311.4 \mu\text{F}\cdot\text{cm}^{-2}$  at 1 mM, reflecting the thickening of the electric double layer due to the adsorption of inhibitor molecules on the steel surface. This results in a reduction in ion flow at the metal/solution interface and enhanced barrier properties.

According to the [Helmholtz model], these trends are ascribed to an increment in the electric double-layer thickness as well as to a local decline in the [dielectric constant] at the HCl/C38 interface.<sup>61,62</sup> This observation highlights the process of the adsorption of inhibitors to the C38 steel surface. In addition, to investigate the impedance diagrams, the EEC (equivalent electrical circuit) pictured in Figure 3 was utilized, consisting of the solution resistance ( $R_s$ ), the charge transfer resistance ( $R_p$ ) and the constant phase angle element (CPE).

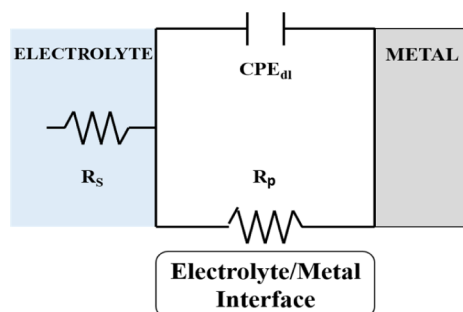


Figure 3. EEC used for modeling the interface C38 steel/1 M HCl.

The presence of a singular constant phase angle element effectively characterizes the interfacial impedance. Additionally, at lower frequency values, the Bode plot illustrates an elevated absolute impedance, indicating enhanced protection that correlates with the concentration of the inhibitor (MPAPB).<sup>45,47,48</sup> Consequently, it can be concluded that the charge transfer process, governed by the dissolution mechanism, is influenced by the concentration of the inhibitor (MPAPB) for both uninhibited and inhibited scenarios using various concentrations.<sup>63</sup> The findings from the electrochemical impedance spectroscopy (EIS) study align with

those previously recorded through potentiodynamic polarization and weight loss methods.

**3.4. Temperature Effect and Thermodynamic Parameters.** Examining the impact of temperature on corrosion kinetics is crucial for comprehending the mode of action and mechanisms involved during the corrosion process. The rise in temperature has a noticeable effect on the dissolution of the film formed by the organic chemicals, leading to a reduction in the C38 corrosion resistance.<sup>64,65</sup> To understand the effect of temperature on the inhibitory efficacy of the used product (MPAPB), polarization data were plotted without and with the addition of 1 mM of the compound (MPAPB) over a range of temperatures (from 293 to 323 K). As shown in Figure 4, the influence of temperature is depicted for both uninhibited conditions and following the addition of 1 mM inhibitor (MPAPB) in 1 M HCl. The corresponding electrochemical values are summarized in Table 5.

According to the findings presented in Table 5,  $i_{\text{corr}}$  (corrosion current density) values show an upward trend with increasing temperatures, irrespective of the existence of an inhibitor in the corrosive solution. The rise in  $i_{\text{corr}}$  displays a constant and significant increase, reflecting the increased metal dissolving with increasing temperature. The inhibitory efficacy of C diminishes as the temperature rises, which is related to the enhanced desorption of the investigated compound first adsorbed on the metallic surface.<sup>66</sup> In conclusion, increasing the temperature reduces the inhibition phenomenon.

The activation energy ( $E_a$ ) was measured based on  $i_{\text{corr}}$  values determined from the polarization curves plotted at different temperatures according to the Arrhenius law (eq 14):<sup>67</sup>

$$\ln(i_{\text{corr}}) = \ln A - \left(\frac{E_a}{R}\right)\frac{1}{T} \quad (14)$$

where  $A$ ,  $R$ , and  $T$  represent the pre-exponential factor of Arrhenius, the ideal gas constant, and the temperature, respectively.

Figure 5 illustrates the Arrhenius plots of  $\ln(i_{\text{corr}})$  vs  $1/T$  for C38 steel in the corrosive environment. The presentation covers both uninhibited conditions (blank) and after adding 1 mM compound (MPAPB).

To derive the standard thermodynamic activation parameters such as  $\Delta H_a^*$  and  $\Delta S_a^*$  of the corrosion process, the transition state equation (eq 15) was utilized:<sup>68</sup>

$$i_{\text{corr}} = \frac{RT}{Nh} \exp\left(\frac{\Delta S_a^*}{R}\right) \exp\left(-\frac{\Delta H_a^*}{RT}\right) \quad (15)$$

here  $R$ ,  $h$ ,  $N$ , and represent the deal gas constant, the Planck constant, Avogadro's number, the activation standard enthalpy, and the activation standard entropy, respectively. The evolution of  $\ln(i_{\text{corr}}/T)$  versus the inverse of temperature is a straight line (Figure 6) with slope =  $-\Delta H_a^*/R$  and  $y$ -intercept =  $\ln \frac{R}{Nh} + \frac{\Delta S_a^*}{R}$ .

These results enabled us to calculate  $E_a$ ,  $\Delta H_a^*$ , and  $\Delta S_a^*$  for C38 steel in the absence and presence of the used inhibitor (MPAPB). Thermodynamic parameter values derived from Figures 5 and 6 are reported in Table 6. An exploration of Table 6 indicates that the positive values reported for the enthalpy demonstrate the endothermic character of the steel dissolution process. Hence, a rise in the values of the activation

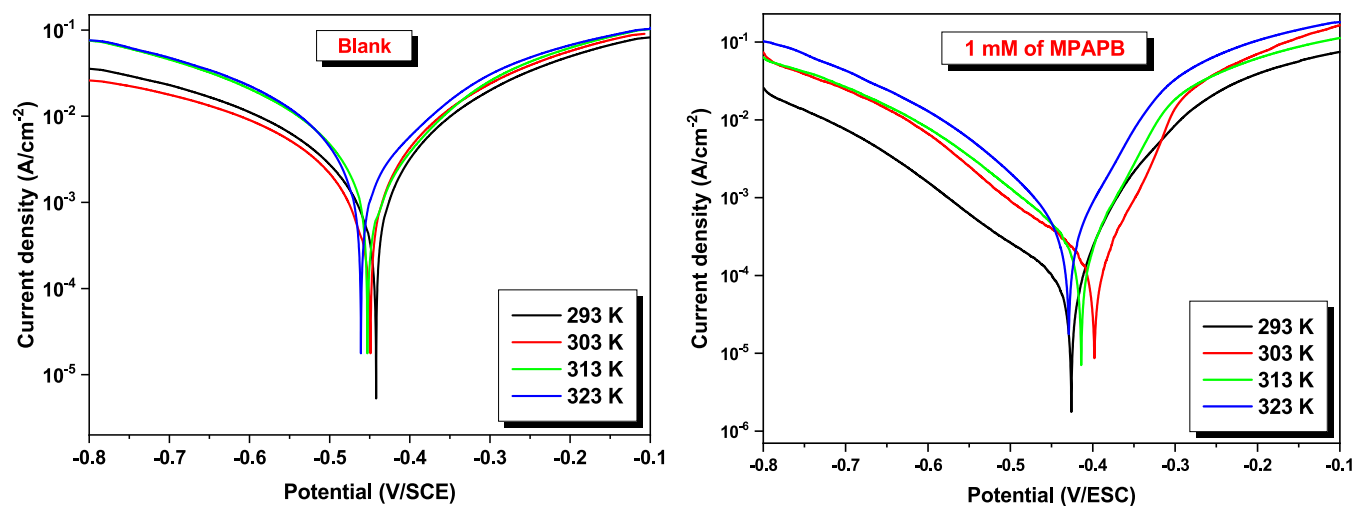


**Figure 4.** Polarization curves of C38 steel in 1 M HCl medium under both uninhibited conditions and the presence of 1 mM inhibitor at various temperatures.

**Table 5.** Electrochemical Parameters of C38 Steel in 1M HCl Solution in the Absence and Presence of 1 mM at Varying Temperatures

| <i>T</i> (K)                                 | $-E_{\text{corr}}$ (mV/SCE) | $i_{\text{corr}}$ ( $\mu\text{A cm}^{-2}$ ) | IE %  | $E_a$ ( $\text{kJ mol}^{-1}$ ) | $\Delta S_a$ ( $\text{J mol}^{-1} \text{K}^{-1}$ ) | $\Delta H_a$ ( $\text{kJ mol}^{-1}$ ) | $E_a - \Delta H_a$ ( $\text{kJ mol}^{-1}$ ) |
|--|-----------------------------|---|-------|--------------------------------|--|---------------------------------------|---|
| (C38 steel/1 M HCl) system                   |                             |   |       |                                |  |                                       |   |
| 293  | 415                         | 879.6                                       | —     | 17.1                           | −139.1   | 14.6                                  | 2.6   |
| 303  | 453                         | 1045.7                                      | —     |                                |  |                                       |   |
| 313  | 449                         | 1164.3                                      | —     |                                |  |                                       |   |
| 323  | 461                         | 17632                                       | —     |                                |  |                                       |   |
| (Inhibitor (MPAPB)/C38 steel/1 M HCl) system |                             |   |       |                                |  |                                       |   |
| 293  | 426                         | 77.6  | 91.18 | 31.8                           | −109.7   | 29.2                                  | 2.6   |
| 303  | 398                         | 94.3  | 90.98 |                                |  |                                       |   |
| 313  | 414                         | 154.6                                       | 86.72 |                                |  |                                       |   |
| 323  | 429                         | 254.7                                       | 85.55 |                                |  |                                       |   |

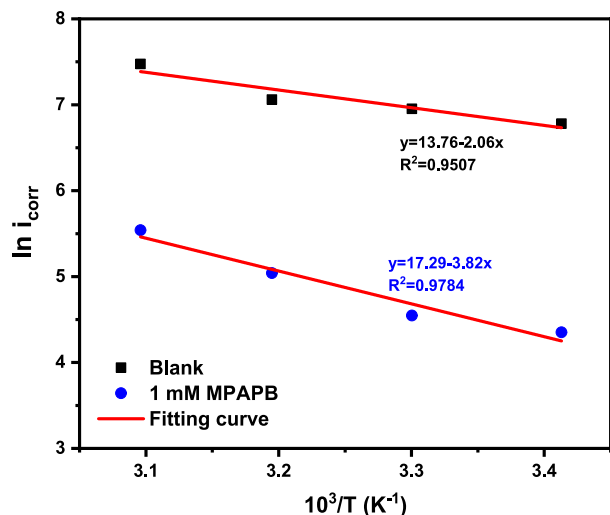


**Figure 5.** Arrhenius plots of  $\ln(i_{\text{corr}})$  vs  $1/T$  for C38 steel in the corrosive environment.

enthalpy is consistent with a drop in C38 dissolution.<sup>54</sup> Furthermore, large negative entropy values suggest a reduction in the disorder when reactants are converted into a complex of activated iron molecules in solution.<sup>69,70</sup>

**3.5. Adsorption Isotherms.** Adsorption isotherms are essential for elucidating the mechanism of electrochemical reactions. Various models, including Langmuir, Frumkin,

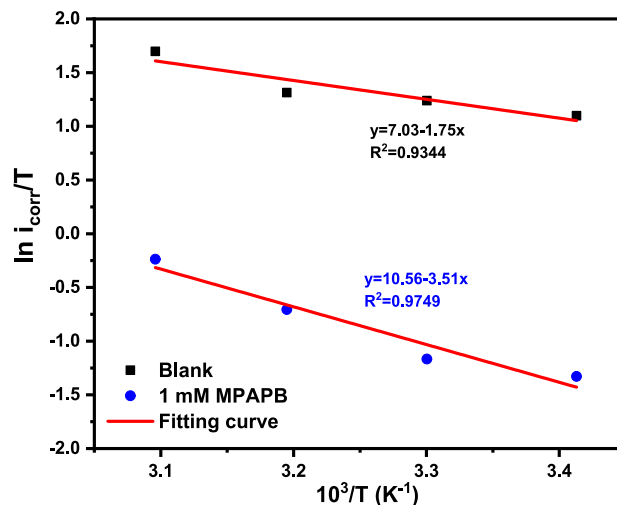


**Figure 6.** Plot of  $\ln(i_{\text{corr}}/T)$  vs  $1/T$  of C38 steel in 1 M HCl before and after adding 1 mM MPAPB compound.

Temkin, etc., are employed to define the relevant mechanism for the studied compound.<sup>55</sup> In this study, the Langmuir isotherm model was determined to be the best fit. Figure 7 displays the curve of  $C_{\text{inh}}/\theta$  as a function of  $C_{\text{inh}}$ , typical of the Langmuir model at 293 K. If it was assumed that the values of IE(%) were not significantly divergent from the impedance

Table 6. GQCD Calculations Utilizing the DFT Method at the B3LYP/6-31G(d,p) basis Set

| $E_{\text{HOMO}}$ (eV) | $E_{\text{LUMO}}$ (eV) | $\Delta E_{\text{gap}}$ (eV) | $\eta$ (eV) | $\omega$ (eV) | $\varepsilon$ (eV <sup>-1</sup> ) | $\chi$ (eV) | $\sigma$ (eV <sup>-1</sup> ) | $\Delta N_{110}$ |
|------------------------|------------------------|------------------------------|-------------|---------------|-----------------------------------|-------------|------------------------------|------------------|
| -5.963                 | 0.640                  | 6.603                        | 3.301       | 1.062         | 0.942                             | 2.648       | 0.303                        | 0.367            |

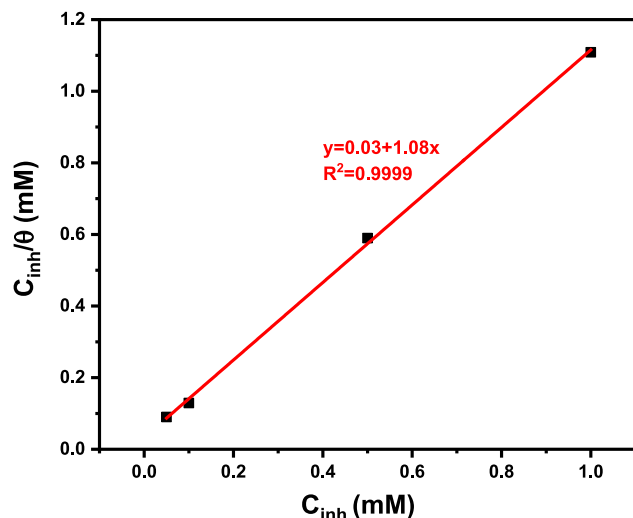


Figure 7. Langmuir adsorption isotherm of the synthesis inhibitor (MPAPB) on C38 steel in 1 M HCl at 293 K.

measurements, then the coverage rate was calculated using eq 16:

$$\frac{C_{\text{inh}}}{\theta} = \frac{1}{K_{\text{ads}}} + C_{\text{inh}} \quad (16)$$

where  $\theta$ ,  $C_{\text{inh}}$ , and  $K_{\text{ads}}$  are the surface coverage degree, the inhibitor concentration, and the equilibrium constant of the adsorption process, respectively.

The  $K_{\text{ads}}$  value serves as an indicator of the degree of adsorption by the organic species onto the C38 surface.<sup>71</sup> To estimate the relevant parameters of adsorption, linear plots were established by means of the least-squares method. Equation 17 relates the  $K_{\text{ads}}$  to the standard free energy of adsorption, as follows:

$$K_{\text{ads}} = \left( \frac{1}{55.5} \right) \exp \left( - \frac{\Delta G_{\text{ads}}^{\circ}}{RT} \right) \quad (17)$$

In general, smaller values of  $\Delta G_{\text{ads}}^{\circ}$  together with a correspondingly high value assigned to  $K_{\text{ads}}$  indicate that the inhibitor is strongly attached to the C38 surface. As is well-known, a  $\Delta G_{\text{ads}}^{\circ}$  inferior to -40 kJ/mol is quoted for chemisorption, suggesting the establishment of chemical bonds between tested organic species and the metal surface.<sup>72</sup> A  $\Delta G_{\text{ads}}^{\circ}$  value of above -20 kJ/mol signifies physisorption, i.e., electrostatic interaction.<sup>73</sup> The  $\Delta G_{\text{ads}}^{\circ}$  value computed for the inhibitor tested (MPAPB) was -16.67 kJ/mol, showing that the physisorption of the inhibitor species on the steel surface.<sup>74</sup>

**3.6. SEM Analysis.** To further explore the protective effect of MPAPB on C38 steel, scanning electron microscopy (SEM) analysis was conducted. SEM images of the steel surface were recorded after 24 h of immersion in 1 M HCl with and without the addition of MPAPB at a concentration of 1 mM, at 303 K. The SEM image of the bare C38 steel surface (Figure 8) before immersion shows a relatively smooth and undamaged surface, with visible scratches from the pretreatment process. After immersion in 1 M HCl, the steel surface exhibits significant

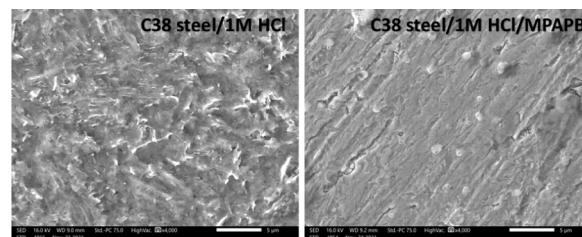


Figure 8. SEM images of mild steel specimens after corrosion in 1 M HCl without and with MPAPB.

corrosion, including deep pits and cavities resulting from the aggressive chloride ions in the solution (Figure 8). However, when MPAPB is added to the acidic medium, the SEM image reveals a surface with much less damage, showing no obvious corrosion pits, indicating that MPAPB effectively mitigates corrosion.

**3.7. Computational Studies.** The density distributions of the highest occupied molecular orbital (HOMO), the lowest unoccupied molecular orbital (LUMO), the optimized geometry structure, and the molecular electrostatic potential (MEP) of the synthesized inhibitor (MPAPB) are displayed in Figure 9. The molecular inhibitor employed contains varying active centers such as carbonyl, aromatic ring, and amide group, which possess pairs of  $\pi$ -electrons  $\pi$  and double and triple bonds, making them active sites for excellent corrosion inhibition.<sup>75</sup> Further, the molecular reactivity of the inhibitor was determined using HOMO and LUMO orbitals. Then,  $E_{\text{HOMO}}$  and  $E_{\text{LUMO}}$  denote the capacity of the synthesized compound to give and receive electrons on the substrate surfaces, respectively. Also, the higher  $E_{\text{HOMO}}$  and lower  $E_{\text{LUMO}}$  values of inhibitory activity indicate a strong electron-donating ability and easier electron accepting, respectively. As shown in Figure 9, the density distribution of the HOMO of the molecule studied (MPAPB) was located and centered on the amide group (electron pairs of the oxygen and nitrogen heteroatoms) and -CH<sub>2</sub>- aliphatic. Then, the density distribution of the LUMO of the molecule used (MPAPB) was located and centered on the carbonyl group (electron pairs of the oxygen atom C=O) and aromatic phenyl ring (double bonds  $\pi$ ).<sup>85</sup> These active centers are responsible for the interactions with the vacant  $d$ -orbitals of the metallic area. Molecular electrostatic potential (MEP) suggests that the electron donor centers (orange to red region) are distributed on the oxygen and nitrogen heteroatoms and some carbon atoms. Then, the acceptor centers (sky to blue region) are distributed on the rest of the inhibitor used (MPAPB). The red regions in the MEP correspond to the density distribution of HOMO, resulting in strong agreement between the MEP and HOMO surface.<sup>76</sup> For global quantum chemical descriptor (GQCD) calculations, see Table 6. As shown in Table 6, the lowest energy gap ( $\Delta E_{\text{gap}}$ ) of the inhibitor studied (MPAPB) indicates more reactivity toward the adsorption on the C38 steel surface. Then, the hardness ( $\eta$ ) value is higher than zero and the lowest softness ( $\sigma$ ), indicating the charge transfer to the inhibitor (MPAPB) followed by back-donation and accepting electrons. Also, the highest electrophilicity ( $\omega$ ) and



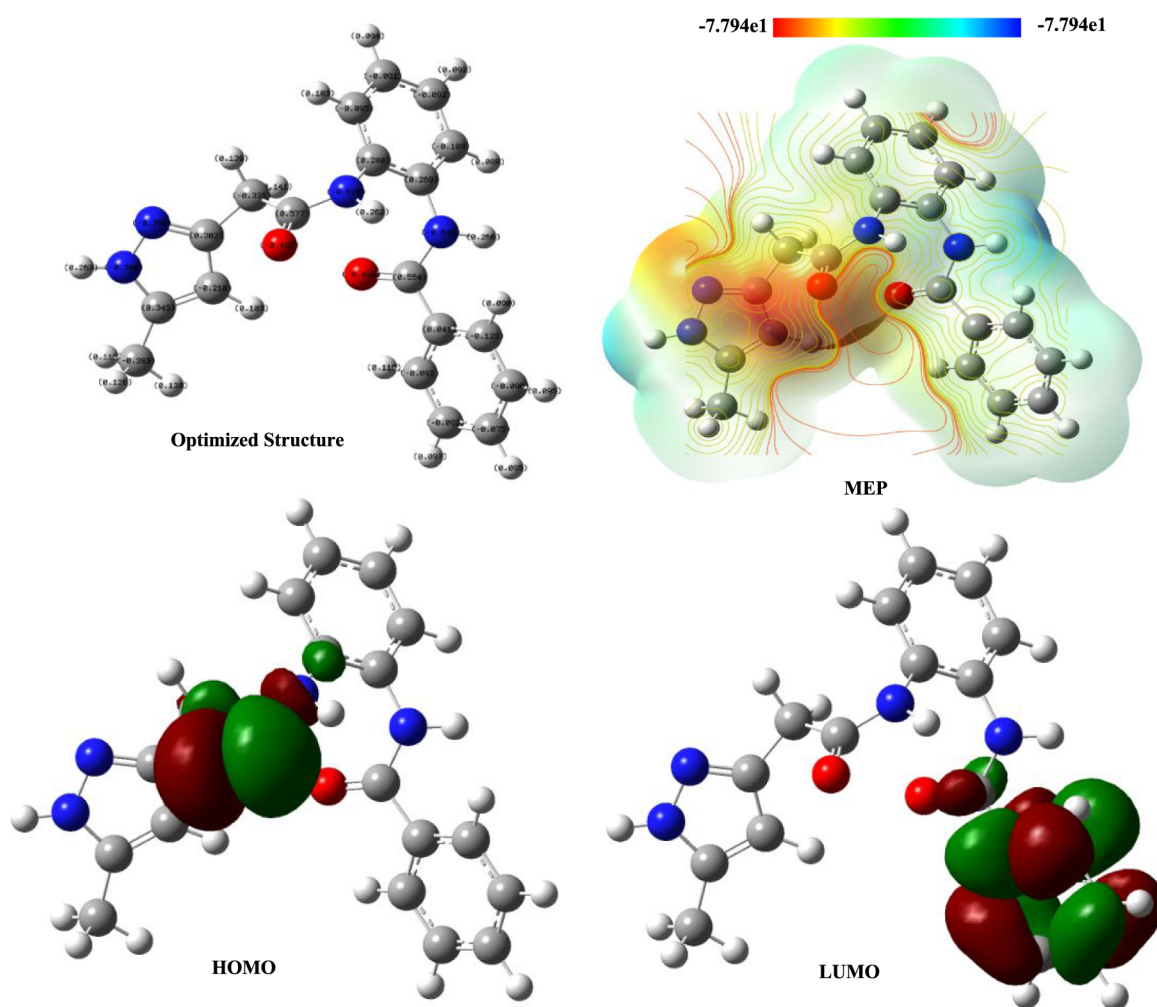


Figure 9. Optimized structure, HOMO, LUMO, and MEP of the studied inhibitor.

Table 7. Fukui Functions and Dual Descriptors for the Most Active Centers of the Inhibitor (MPAPB)

| site | $f_k^+$  | $f_k^-$  | $\sigma_k^+$ | $\sigma_k^-$ | $\omega_k^+$ | $\omega_k^-$ | $f_k^2$ | $\Delta\sigma_k$ | $\Delta\omega_k$ |
|------|----------|----------|--------------|--------------|--------------|--------------|---------|------------------|------------------|
| C2   | 0.02138  | -0.03674 | 0.00648      | -0.01113     | 0.02271      | -0.03902     | 0.05812 | 0.01761          | 0.06173          |
| C6   | -0.00804 | -0.05654 | -0.00244     | -0.01713     | -0.00854     | -0.06005     | 0.0485  | 0.01469          | 0.05151          |
| C12  | 0.00982  | -0.05741 | 0.00298      | -0.0174      | 0.01043      | -0.06097     | 0.06723 | 0.02038          | 0.0714           |
| C18  | 0.35353  | -0.37088 | 0.10712      | -0.11238     | 0.37545      | -0.39387     | 0.72441 | 0.2195           | 0.76932          |
| C19  | 0.02404  | -0.02213 | 0.00728      | -0.00671     | 0.02553      | -0.0235      | 0.04617 | 0.01399          | 0.04903          |
| O29  | -0.02328 | -0.03735 | -0.00705     | -0.01132     | -0.02472     | -0.03967     | 0.01407 | 0.00427          | 0.01495          |
| C33  | 0.37854  | -0.15181 | 0.1147       | -0.046       | 0.40201      | -0.16122     | 0.53035 | 0.1607           | 0.56323          |
| C35  | -0.10043 | -0.1272  | -0.03043     | -0.03854     | -0.10666     | -0.13509     | 0.02677 | 0.00811          | 0.02843          |
| N39  | -0.01561 | -0.05768 | -0.00473     | -0.01748     | -0.01658     | -0.06126     | 0.04207 | 0.01275          | 0.04468          |

lowest nucleophilicity ( $\varepsilon$ ) values suggest the higher capacity of inhibitors to accept electrons. From Table 6, the electrons transferred from the inhibitor to metal lower than 3.6 ( $\Delta N_{110} < 3.6$ ) indicates a higher susceptibility to give electrons to the metallic surface.<sup>77</sup>

**3.8. Fukui Function Descriptors.** The electrophilic and nucleophilic functions ( $f_k^+$  and  $f_k^-$ ), the local electrophilicity ( $\omega_k^+$  and  $\omega_k^-$ ), the local softness ( $\sigma_k^+$  and  $\sigma_k^-$ ), the dual Fukui function ( $f_k^2$ ), the dual local softness ( $\Delta\sigma_k$ ), and the philicity ( $\Delta\omega_k$ ) of the inhibitor (MPAPB) were calculated according to eqs 18–24:<sup>78–80</sup>

$$f_k^+ = P_k(N+1) - P_k(N) \quad (18)$$

$$f_k^- = P_k(N) - P_k(N-1) \quad (19)$$

$$\sigma_k^\pm = \sigma f_k^\pm \quad (20)$$

$$\omega_k^\pm = \omega f_k^\pm \quad (21)$$

$$f_k^2 = f_k^+ - f_k^- \quad (22)$$

$$\Delta\sigma_k = \sigma_k^+ - \sigma_k^- \quad (23)$$

$$\Delta\omega_k = \omega_k^+ - \omega_k^- \quad (24)$$

The main active sites identified are given in Table 7 and Figure 10.

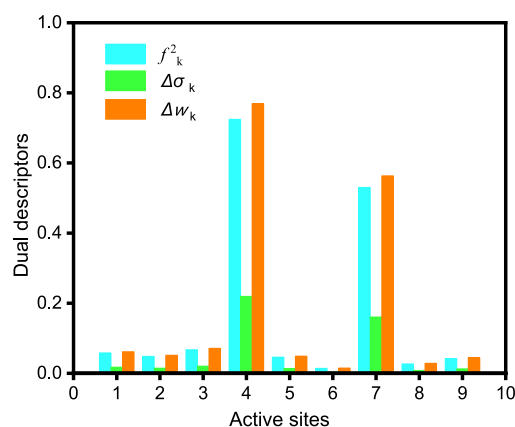


**Figure 10.** Graphical representation of dual descriptors ( $f_k^2$ ,  $\Delta\sigma_k$ , and  $\Delta\omega_k$ ) for the main active centers of inhibitor (MPAPB).

As shown in Table 7, the electrophilic function displays maximum values at the active sites as follows: C2 (0.02138), C18 (0.35353), C19 (0.02404), and C33 (0.37854). Further, the highest values of the local softness and local electrophilicity  $\omega^+$  for the active sites are located at the same carbon atoms, such as C2, C12, C18, C19, and C33. These active sites are favorable for nucleophilic attacks.<sup>78,81</sup> According to the data in Table 7, the main active sites have  $f_k^2$ ,  $\Delta\sigma_k$ , and  $\Delta\omega_k$  values greater than zero. These results suggest that the synthesized product (MPAPB) can donate electrons to the C38 surface, confirming that these active sites are favorable for electrophilic attack.<sup>82,83</sup>

**3.9. MD Simulation.** MD simulation provides valuable insights into the interaction and behavior of the inhibitor at the molecular level on a metallic surface. MD simulation was realized through the Forcite module of Materials Studio software, which was developed by BIOVIA Inc.<sup>84,85</sup> at varying temperatures (293, 303, 313, and 323 K). The dynamic process was carried out until the entire system achieved a state of equilibrium, characterized by a balanced temperature and energy within the system. The equilibrium adsorption configuration (top and side views) of macromolecule resins on the iron surface (Fe(110)) at 293 K is displayed in Figure 11a. As shown in Figure 11a, the macromolecule resins can be

adsorbed on the metallic area owing to nitrogen and oxygen atoms and also the double bonds of aromatic rings.<sup>37</sup> Figure 11b displays the density field distribution of macromolecular resins on the Fe(110) surface. It can be inferred that a dense barrier layer is likely formed in the three-dimensional space, contributing to the resistance against corrosion and providing effective anticorrosive protection. The adsorption energy ( $E_{\text{ads}}$ ) was calculated as a function of the following eq 25:

$$E_{\text{ads}} = E_{\text{total}} - (E_{\text{surf+solu}} + E_{\text{inh+solu}}) + E_{\text{solu}} \quad (25)$$

where  $E_{\text{total}}$ ,  $E_{\text{surf+solu}}$ ,  $E_{\text{inh+solu}}$ , and  $E_{\text{solu}}$  are the total energy, which includes iron crystal, the adsorbed inhibitor macromolecule resins, the potential energies of the system uninhibited, the potential energies of the system inhibited without the iron crystal, and the potential energy of the  $\text{H}_2\text{O}$ , respectively. The adsorption energies were derived from the average adsorption energies of the obtained equilibrium configurations. From Figure 11c, the extracted  $E_{\text{ads}}$  values are −832.1, −829.3, −815.2, and −804.7 kJ/mol at temperatures of 293, 303, 313, and 323 K, respectively. These data reveal that at all observed temperatures, the adsorption energies are negative, indicating a spontaneous adsorption process. Typically, a more negative value of  $E_{\text{ads}}$  suggests a stronger adsorption interaction between macromolecular resins and the metallic surface.<sup>55</sup> It appears that the absolute  $E_{\text{ads}}$  values decrease with increasing temperatures, which is consistent with the order of the observed anticorrosive performance.<sup>2</sup>

**3.10. Mechanism of Adsorption and Inhibition.** The adsorption and inhibition effects of MPAPB on the C38 steel surface in 1 M HCl can be understood through experimental and theoretical findings. It is well-established that MPAPB inhibits corrosion by adsorbing onto the steel surface, a process that depends on the molecular structure of MPAPB and the surface characteristics of the steel. The adsorption of MPAPB onto the metal occurs via interactions involving the unshared electron pairs of heteroatoms (such as nitrogen and oxygen) as well as the  $\pi$ -electrons of aromatic rings, which interact with the vacant d-orbitals of surface iron atoms. In the presence of MPAPB, adsorption on the C38 steel follows a mechanism similar to that depicted in Figure 12, where the inhibitor molecules create a barrier that protects the steel from the corrosive action of chloride ions ( $\text{Cl}^-$ ). The active adsorption

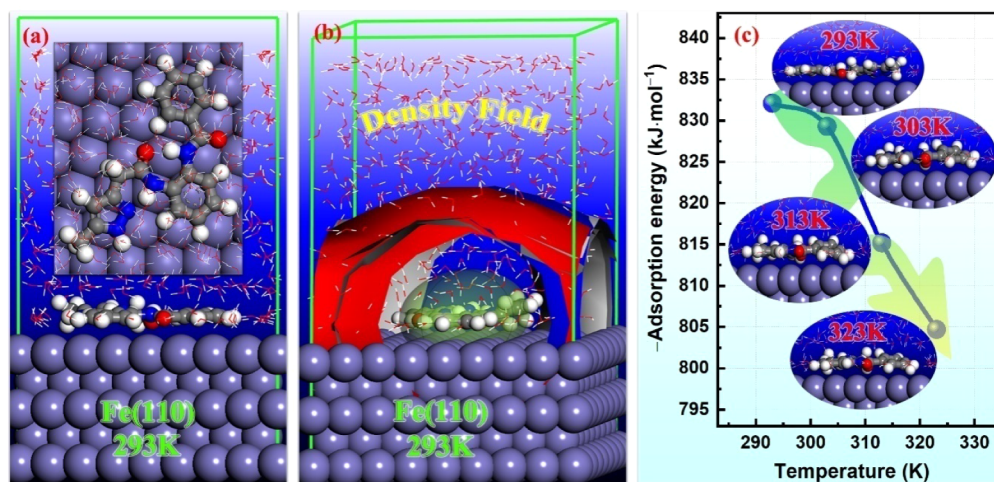


**Figure 11.** (a) Equilibrium adsorption configuration of MPAPB on the Fe(110) surface; (b) density field distribution, and (c) dependence of adsorption energy on temperature.

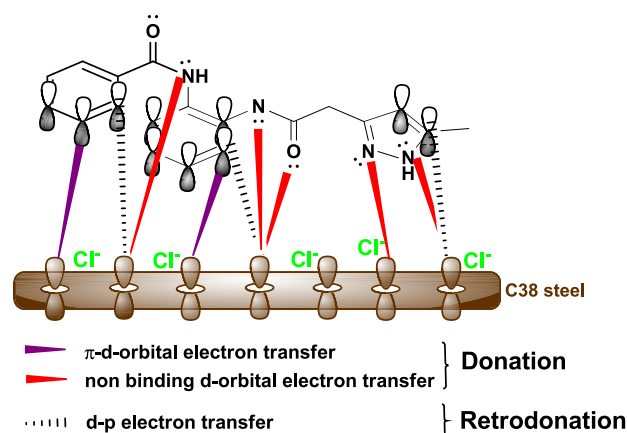


Figure 12. Suggested mechanism of MPAPB on the C38 steel surface.

sites, which include the lone pairs on heteroatoms and delocalized  $\pi$ -electrons in unsaturated and aromatic regions, are crucial for the formation of a stable protective layer. MPAPB contains heteroaromatic and aromatic rings and nitrogen and oxygen atoms, which play a vital role in bonding with the steel surface during adsorption. This interaction forms coordination bonds between MPAPB and the iron atoms, thus shielding the steel from further corrosive attack.

#### 4. CONCLUSION

The aim of this study is to assess the corrosion inhibition efficacy of *N*-{2-[2-(5-methyl-1*H*-pyrazol-3-yl)acetamido]-phenyl}benzamide monohydrate (MPAPB) as a newly synthesized inhibitor for the corrosion of C38 steel in 1 M HCl. Potentiodynamic polarization (PDP) results revealed that MPAPB acts as a mixed-type inhibitor, effectively reducing both anodic and cathodic reactions, thereby offering complete protection against corrosion. Electrochemical impedance spectroscopy (EIS) outcomes showed that the addition of MPAPB increased the polarization resistance ( $R_p$ ) values while decreasing the double-layer capacitance ( $C_{dl}$ ), indicating that the inhibitor molecules adsorb onto the metal surface, forming a protective layer. At a concentration of 1 mM, MPAPB exhibited a corrosion inhibition efficiency (IE%) of 90.2%. Additionally, the introduction of MPAPB resulted in a significant decrease in current density, from  $879.6 \mu\text{A}\cdot\text{cm}^{-2}$  in the blank solution to  $77.6 \mu\text{A}\cdot\text{cm}^{-2}$  at a 1 mM concentration at 293 K, as observed from the PDP findings. Moreover, DFT calculations and MD simulations were conducted to simulate the interaction between the inhibitor and the iron surface. The agreement between the calculated and experimental outcomes validates the theoretical models and enhances our confidence in understanding the inhibitory behavior. Several directions for further investigation are proposed to provide a broader context for this study and guide future research. First, exploring the performance of MPAPB in more aggressive corrosive environments, such as higher concentrations of HCl or the presence of other industrial corrosive agents, would help assess its efficacy under more challenging conditions. Furthermore, advanced computational studies, including molecular dynamics simulations at different temperatures, could provide a better understanding of the interaction mechanisms of the inhibitor and optimize its design for industrial applications.

#### ■ ASSOCIATED CONTENT

##### Supporting Information

The Supporting Information is available free of charge at <https://pubs.acs.org/doi/10.1021/acsomega.4c11555>.

$^1\text{H}$  and  $^{13}\text{C}$  NMR data, IR spectrum, and mass spectrum (ESI) for *N*-{2-[2-(5-methyl-1*H*-pyrazol-3-yl)-acetamido]phenyl}benzamide monohydrate (MPAPB) (Figures S1–S4) (PDF)

#### ■ AUTHOR INFORMATION

##### Corresponding Author

Nada Kheira Sebbar – Department of Applied Chemistry, Faculty of Applied Sciences Ait Melloul, Ibn Zohr University, Agadir 00000, Morocco; Laboratory of Plant Chemistry, Organic and Bioorganic Synthesis, Faculty of Sciences, Mohammed V University in Rabat, Rabat 10500, Morocco; [orcid.org/0000-0003-4944-1010](https://orcid.org/0000-0003-4944-1010); Email: [n.sebbar@uiz.ac.ma](mailto:n.sebbar@uiz.ac.ma)

##### Authors

Karim Azgaou – Laboratory of Spectroscopy, Molecular Modelling Materials, Nanomaterial Water and Environment – CERNE2D, Faculty of Sciences and Environment, Materials and Sustainable Development Team – CERNE2D, High School of Technology, Mohammed V University in Rabat, Rabat 10500, Morocco

Rachid Hsissou – Laboratory of Organic Chemistry, Bioorganic and Environment, Chemistry Department, Faculty of Sciences, Chouaib Doukkali University, El Jadida 00000, Morocco; [orcid.org/0000-0003-3080-5021](https://orcid.org/0000-0003-3080-5021)

Karim Chkirate – Laboratory of Heterocyclic Organic Chemistry, Pharmacochimie Competence Center, Mohammed V University in Rabat, Rabat 10500, Morocco

Mohammed Benmessaoud – Environment, Materials and Sustainable Development Team – CERNE2D, High School of Technology, Mohammed V University in Rabat, Rabat 10500, Morocco

Mohamed Hefnawy – Department of Pharmaceutical Chemistry, College of Pharmacy, King Saud University, Riyadh 11451, Saudi Arabia

Ali El Gamal – Department of Pharmacognosy, College of Pharmacy, King Saud University, Riyadh 11451, Saudi Arabia

Hicham Elmsellem – Laboratory of Applied Chemistry and Environment (LCAE). Department of Chemistry, Faculty of Sciences, University Mohamed I, Oujda 00000, Morocco; Higher Institute of Nursing Professions and Health Techniques (ISPITSO), Oujda 63303, Morocco

Lei Guo – School of Material and Chemical Engineering, Tongren University, Tongren 554300, China

El Mokhtar Essassi – Laboratory of Heterocyclic Organic Chemistry, Pharmacochimie Competence Center, Mohammed V University in Rabat, Rabat 10500, Morocco

Soud El Hajjaji – Laboratory of Spectroscopy, Molecular Modelling Materials, Nanomaterial Water and Environment – CERNE2D, Faculty of Sciences, Mohammed V University in Rabat, Rabat 10500, Morocco

Complete contact information is available at: <https://pubs.acs.org/doi/10.1021/acsomega.4c11555>



## Funding

This study was funded by the Researchers Supporting Project (number RSPD2024R754), King Saud University, Riyadh, Saudi Arabia.

## Notes

The authors declare no competing financial interest.

## ACKNOWLEDGMENTS

The authors acknowledge the financial support through the Researchers Supporting Project number (RSPD2024R754), King Saud University, Riyadh, Saudi Arabia.

## REFERENCES

- (1) Taia, A.; El Ibrahim, B.; Benhiba, F.; Ashfaq, M.; Tahir, M. N.; Essaber, M.; Aatif, M.; Hökelek, T.; Mague, J. T.; Sebbar, N. K.; Essassi, E. M. Single Crystal X-ray Structure, Hirshfeld Surface Analyses, DFT Computations, and Monte Carlo Simulations of New Eugenol Derivatives Bearing 1,2,3-triazole Moiety. *J. Mol. Struct.* **2021**, 1234, 130189.
- (2) Chkirate, K.; Azgaou, K.; Elmsellem, H.; Ibrahim, B. E.; Sebbar, N. K.; Anouar, E. H.; Benmessaoud, M.; El Hajjaji, S.; Essassi, E. M. Corrosion inhibition potential of 2-[(5-methylpyrazol-3-yl)methyl]-benzimidazole against carbon steel corrosion in 1 M HCl solution: Combining experimental and theoretical studies. *J. Mol. Liq.* **2021**, 321, 114750.
- (3) Hni, B.; Sebbar, N. K.; Anouar, E. H.; El Ibrahim, B.; Ellouz, M.; Hökelek, T.; Mague, J. T.; Urrutigoity, M.; Ahabchane, N. H.; Essassi, E. M. Crystal Structures, Spectroscopic Characterizations, DFT Calculations, Hirshfeld Surface Analyses, and Monte Carlo Simulations of Novel Long-chain Alkyl-substituted 1,4-benzothiazine Derivatives. *J. Mol. Struct.* **2020**, 1221, 128886.
- (4) Lahmidi, S.; El Youssfi, A.; Dafali, A.; Elmsellem, H.; Sebbar, N. K.; El Ousif, L.; Jilalat, A. E.; El Mahi, B.; Essassi, E. M.; Abdel-Rahman, I.; Hammouti, B. Corrosion inhibition of mild steel by two new 1, 2, 4-triazolo [1, 5-a] pyrimidine derivatives in 1 M HCl: Experimental and computational study. *J. Mater. Environ. Sci.* **2017**, 8, pp. 225–237.
- (5) Sghyar, R.; Basavarajaiah, S. M.; Chda, A.; Moussaoui, O.; El Hadrami, E. M.; Ben-Tama, A.; Aarab, L.; Mague, J. T.; Prashantha, K.; Javeed, M.; Sebbar, N. K.; Essassi, E. M.; Javeed, M. Design, synthesis, biological evaluation on immune cell proliferation, crystal structures, spectroscopic characterizations, DFT calculations, ADME analysis, and molecular docking studies with COX of novel tetrazole-Galactopyranosyl analogues. *J. Mol. Struct.* **2023**, 1287, 135695.
- (6) Azgaou, K.; Damej, M.; El Hajjaji, S.; Sebbar, N. K.; Elmsellem, H.; El Ibrahim, B.; Benmessaoud, M. Synthesis and characterization of N-(2-aminophenyl)-2-(5-methyl-1H-pyrazol-3-yl) acetamide (AMPA) and its use as a corrosion inhibitor for C38 steel in 1 M HCl. Experimental and theoretical study. *J. Mol. Struct.* **2022**, 1266, 133451.
- (7) Essassi, E. M.; Baba, Y. F.; Sebbar, N. K.; Elmsellem, H.; Rodi, Y. K.; Chraïbi, M.; Benbrahim, K. F.; Fouad, Q. C.; Nikolova, M. P.; Steli, H. Effects of 6-substituted-2-oxo-1, 2-dihydroquinoline-4-carboxylic acid derivatives on mild steel corrosion in hydrochloric acid solution: Experimental and theoretical studies, and their antibacterial activity. *Eur. J. Chem.* **2017**, 1, 1, pp. 1–11.
- (8) Hsissou, R.; Bekhta, A.; Elharfi, A.; Benzidia, B.; Hajjaji, N. Theoretical and Electrochemical Studies of the Coating Behavior of a New Epoxy Polymer: Hexaglycidyl Ethylene of Methylene Dianiline (HGEMDA) on E24 Steel in 3.5% NaCl. *Port. Electrochim. Acta* **2018**, 36, 101–117.
- (9) Hsissou, R.; Benzidia, B.; Hajjaji, N.; Elharfi, A. E. Electrochemical Investigation, and Morphological Study of the Coating Behavior of a New Polymeric Polyeepoxide Architecture: Crosslinked and Hybrid Decaglycidyl of Phosphorus Penta Methylene Dianiline on E24 Carbon Steel in 3.5% NaCl. *Port. Electrochim. Acta* **2019**, 37 (3), 179–191.
- (10) Elmsellem, H.; Harit, T.; Aouniti, A.; Malek, F.; Riahi, A.; Chetouani, A.; Hammouti, B. Adsorption Properties and Inhibition of Mild Steel Corrosion in 1 M HCl Solution by Some Bipyrazolic Derivatives: Experimental and Theoretical Investigations. *Prot. Met. Phys. Chem. Surf.* **2015**, 51, 873–884.
- (11) Hayani, S.; Thiruvalluvar, A. A.; Baba, Y. F.; Rodi, Y. K.; Muthunatesan, S.; Chahdi, F. O.; Mague, J. T.; Ibrahim, B. E.; Anouar, E. H.; Sebbar, N. K.; Essassi, E. M. Structure Elucidation Hirshfeld Surface Analysis, DFT, Molecular Docking, and Monte Carlo Simulation of New Quinoline-4-carboxylate Derivatives. *J. Mol. Struct.* **2021**, 1234, 130195.
- (12) Hayani, S.; Sert, Y.; Baba, Y. F.; Benhiba, F.; Chahdi, F. O.; Laraoui, F.-Z.; Mague, J. T.; El Ibrahim, B.; Sebbar, N. K.; Rodi, Y. K.; Essassi, E. M. New Alkyl (Cyclohexyl) 2-oxo-1-(prop-2-yn-1-yl)-1,2-dihydroquinoline-4-carboxylates: Synthesis, Crystal Structure, Spectroscopic Characterization, Hirshfeld Surface Analysis, Molecular Docking Studies, and DFT Calculations. *J. Mol. Struct.* **2021**, 1227, 129520.
- (13) Chkirate, K.; Sebbar, N. K.; Hökelek, T.; Krishnan, D.; Mague, J. T.; Essassi, E. M. Crystal Structure and Hirshfeld Surface Analysis of (4Z)-1-butyl-4-(2-oxopropylidene)-2,3,4,5-tetrahydro-1H-1,5-benzodiazepin-2-one. *Acta Crystallogr. Sect. E Crystallogr. Commun.* **2018**, 74, 1669–1673.
- (14) Sbair, F.; Chkirate, K.; Regragui, R.; Essassi, E.; Pierrot, M. Diaquabis {2-[(5-methylpyrazol-3-yl)methyl]benzimidazole} Nickel (II) Dichloride Dihydrate. *Acta Crystallogr., Sect. E: Struct. Rep. Online* **2002**, 58, m337–m339.
- (15) Chkirate, K.; Karrouchi, K.; Dege, N.; Sebbar, N. K.; Ejjoumany, A.; Radi, S.; Adarsh, N. N.; Talbaoui, A.; Ferbinteanu, M.; Essassi, E. M.; Garcia, Y. Co(II) and Zn(II) Pyrazolyl-benzimidazole Complexes with Remarkable Antibacterial Activity. *New J. Chem.* **2020**, 44 (6), 2210–2221.
- (16) Chkirate, K.; Fettach, S.; Karrouchi, K.; Sebbar, N. K.; Essassi, E. M.; Mague, J. T.; Radi, S.; Faouzi, M. E. A.; Adarsh, N. N.; Garcia, Y. Novel Co(II) and Cu(II) Coordination Complexes Constructed from Pyrazole-acetamide: Effect of Hydrogen Bonding on the Self-assembly Process and Antioxidant Activity. *J. Inorg. Biochem.* **2019**, 191, 21–28.
- (17) Chkirate, K.; Regragui, R.; Essassi, E. M.; Pierrot, M. Crystal Structure of Diaquabis [N-2-aminophenyl-5-methylpyrazol-yl Acetamido] Zinc (II) Diperchlorate, C<sub>24</sub>H<sub>34</sub>N<sub>8</sub>O<sub>4</sub>Zn(ClO<sub>4</sub>)<sub>2</sub>. *Z. Kristallogr. New Cryst. Struct.* **2001**, 216, pp. 635–636.
- (18) Beloglazov, S. M.; Dzhaferov, Z. I.; Polyakov, V. N.; Demushin, N. N. Quaternary Ammonium Salts as Corrosion Inhibitors of Steel in the Presence of Sulfate-reducing Bacteria. *Prot. Met.* **1991**, 27, pp. 810–813.
- (19) Park, K.; Lee, B. M.; Hyun, K. H.; Han, T.; Lee, D. H.; Choi, H. H. Design and Synthesis of Acetylenyl Benzamide Derivatives as Novel Glucokinase Activators for the Treatment of T2DM. *ACS Med. Chem. Lett.* **2015**, 6, 296–301.
- (20) Sethi, R.; Jain, S.; Arora, S.; Saini, D.; Jain, N. Characterization and Molecular Docking Studies of Novel N-(Benzimidazol-1-ylmethyl)-4-chlorobenzamide Analogues for Potential Anti-inflammatory and Antimicrobial Activity. *Anti-Inflamm. Anti-Allergy Agents Med. Chem.* **2018**, 17 (1), 16–31.
- (21) Thirumurugan, K.; Lakshmanan, S.; Govindaraj, D.; Prabu, D. S. D.; Ramalakshmi, N.; Antony, S. A. D. Synthesis, and Anti-inflammatory Activity of Pyrimidine Scaffold Benzamide Derivatives as Epidermal Growth Factor Receptor Tyrosine Kinase Inhibitors. *J. Mol. Struct.* **2018**, 1171, 541–550.
- (22) Bouabdallah, I.; M'Barek, L. A.; Ziad, A.; Ramdani, A.; Zidane, I.; Melhaoui, A. Anticancer effect of three pyrazole derivatives. *Nat. Prod. Res.* **2006**, 20 (11), 1024–1030.
- (23) Bennani, F. E.; Doudach, L.; Cherrah, Y.; Raml, Y.; Karrouchi, K.; Ansar, H.; Faouzi, M. E. A. Overview of recent developments of pyrazole derivatives as an anticancer agent in different cell line. *Bioorg. Chem.* **2020**, 97, 103470.
- (24) Cherrak, K.; Khamaysa, O. M. A.; Bidi, H.; El Massaoudi, M.; Ali, I. A.; Radi, S.; El Ouadi, Y.; El-Hajjaji, F.; Zarrouk, A.; Dafali, A.



Performance evaluation of newly synthesized bi-pyrazole derivatives as corrosion inhibitors for mild steel in acid environment. *J. Mol. Struct.* **2022**, *1261*, 132925.

(25) Verma, C.; Saji, V. S.; Quraishi, M. A.; Ebenso, E. E. Pyrazole derivatives as environmental benign acid corrosion inhibitors for mild steel: Experimental and computational studies. *J. Mol. Liq.* **2020**, *298*, 111943.

(26) El Arrouji, S.; Karrouchi, K.; Berisha, A.; Alaoui, K. I.; Warad, I.; Rais, Z.; Radi, S.; Taleb, M.; Ansar, M.; Zarrouk, A. New pyrazole derivatives as effective corrosion inhibitors on steel-electrolyte interface in 1 M HCl: Electrochemical, surface morphological (SEM) and computational analysis. *Colloids Surf., A* **2020**, *604*, 125325.

(27) Mechbal, N.; Belghiti, M. E.; Benzbiria, N.; Lai, C. H.; Kaddouri, Y.; Karzazi, Y.; Touzani, R.; Zertoubi, M. Correlation between corrosion inhibition efficiency in sulfuric acid medium and the molecular structures of two newly eco-friendly pyrazole derivatives on iron oxide surface. *J. Mol. Liq.* **2021**, *331*, 115656.

(28) Bima, D. N.; Muhtar, H.; Darmawan, A. Comprehensive investigation of a new pyrazole derivative Schiff base complex: Revealing its potent protection against carbon steel corrosion. *Chem. Eng. Res. Des.* **2024**, *208*, 313–325.

(29) Matine, A.; Es-Sounni, B.; Bakhouch, M.; Bahkali, A. H.; El Abdallaoui, H. E. A.; Wang, S.; Syed, A.; Wong, L. S.; Saleh, N.; Zeroual, A. Design, synthesis, and evaluation of a pyrazole-based corrosion inhibitor: a computational and experimental study. *Sci. Rep.* **2024**, *14* (1), 25238.

(30) Adlani, L.; Benzbiria, N.; Titi, A.; Timoudan, N.; Warad, I.; AlObaid, A.; Al-Maswari, B. M.; Benhiba, F.; Touzani, R.; Zarrok, H.; Bentiss, F.; Oudda, H.; Zarrouk, A. Adsorption and Inhibition Mechanisms of New Pyrazole Derivatives for Carbon Steel Corrosion in Hydrochloric Acid Solutions Based on Experimental, Computational, and Theoretical Calculations. *ACS Omega* **2024**, *9* (12), 13746–13763.

(31) Al Jahdaly, B. A.; Masaret, G. S. Synthesis and inhibitive behavior of new thiazolyl-pyrazole derivative at low carbon steel/HCl interface: Electrochemical, morphology and theoretical investigations. *J. Mol. Liq.* **2022**, *364*, 119933.

(32) El Hajjaji, F.; Abridgach, F.; Hamed, O.; Hasan, A. R.; Taleb, M.; Jodeh, S.; Rodríguez-Castellón, E.; Del Valle Martínez de Yuso, M.; Algarra, M. Corrosion resistance of mild steel coated with organic material containing pyrazol moiety. *Coatings* **2018**, *8* (10), 330.

(33) Chkirate, K.; Kansiz, S.; Karrouchi, K.; Mague, J. T.; Dege, N.; Essassi, E. M. Crystal Structure and Hirshfeld Surface Analysis of N-{2-[(E)-(4-methylbenzylidene) Amino] Phenyl}-2-(S-methyl-1-H-pyrazol-3-yl) Acetamide Hemihydrate. *Acta Crystallogr., Sect. E: crystallogr. Commun.* **2019**, *75*, 154–158.

(34) Chkirate, K.; Kansiz, S.; Karrouchi, K.; Mague, J. T.; Dege, N.; Essassi, E. M. Crystal Structure and Hirshfeld Surface Analysis of a New Benzodiazepine Derivative: 4-dichloromethyl-2,3-dihydro-1H-1,5-benzodiazepin-2-one. *Acta Crystallogr., Sect. E: crystallogr. Commun.* **2019**, *75*, 33–37.

(35) Hsissou, R.; Abbout, S.; Safi, Z.; Benhiba, F.; Wazzan, N.; Guo, L.; Nouneh, K.; Briche, S.; Erramli, H.; Ebn Touhami, M.; Assouag, M.; Elharfi, A. Synthesis and Anticorrosive Properties of Epoxy Polymer for CS in [1 M] HCl Solution: Electrochemical, AFM, DFT and MD Simulations. *Constr. Build. Mater.* **2021**, *270*, 121454.

(36) Becke, A. D. A New Mixing of Hartree–Fock and Local Density-functional Theories. *J. Chem. Phys.* **1993**, *98*, 1372–1377.

(37) Parr, R.; Yang, W. *Density-functional Theory of Atoms and Molecules*; Oxford University Press: Oxford, 1989.

(38) Lee, C.; Yang, W.; Parr, R. G. Development of the Colle-Salvetti Correlation-energy Formula into a Functional of the Electron Density. *Phys. Rev. B* **1988**, *37*, 785.

(39) Frisch, A. et al. *Gaussian 09w Reference*; Gaussian Inc.: Wallingford, USA, 2009; p 25.

(40) Guo, L.; Safi, Z. S.; Kaya, S.; Shi, W.; Tüzün, B.; Altunay, N.; Kaya, C. Anticorrosive Effects of Some Thiophene Derivatives Against

the Corrosion of Iron: A Computational Study. *Front. Chem.* **2018**, *6*, 155.

(41) Benhiba, F.; Hsissou, R.; Benzekri, Z.; Belghiti, M. E.; Lamhamdi, A.; Bellaouchou, A.; Guenbour, A.; Boukhris, S.; Oudda, H.; Warad, I.; Zarrouk, A. Nitro Substituent Effect on the Electronic Behavior and Inhibitory Performance of Two Quinoxaline Derivatives in Relation to the Corrosion of Mild Steel in 1 M HCl. *J. Mol. Liq.* **2020**, *312*, 113367.

(42) Benahmed, M.; Djeddi, N.; Akkal, S.; Laouar, H. Saccocalyx Satureioides as Corrosion Inhibitor for Carbon Steel in Acid Solution. *Int. J. Ind. Chem.* **2016**, *7*, 109–120.

(43) Mahdavian, M.; Ashhari, S. Corrosion Inhibition Performance of 2-Mercaptobenzimidazole and 2-Mercaptobenzoxazole Compounds for Protection of Mild Steel in Hydrochloric Acid Solution. *Electrochim. Acta* **2010**, *55*, 1720–1724.

(44) Elmsellem, H.; Nacer, H.; Halaimia, F.; Aouniti, A.; Lakehal, I.; Chetouani, A.; Al-Deyab, S.; Warad, I.; Touzani, R.; Hammouti, B. Anti-corrosive Properties and Quantum Chemical Study of (E)-4-methoxy-N-(methoxybenzylidene) Aniline and (E)-N-(4-methoxybenzylidene)-4-nitroaniline Coating on Mild Steel in Molar Hydrochloric Acid. *Int. J. Electrochem. Sci.* **2014**, *9*, 5328–5535.

(45) Salarvand, Z.; Amirnasr, M.; Talebian, M.; Raeissi, K.; Meghdadi, S. Enhanced Corrosion Resistance of Mild Steel in 1 M HCl Solution by Trace Amount of 2-phenyl-benzothiazole Derivatives: Experimental, Quantum Chemical Calculations, and Molecular Dynamics (MD) Simulation Studies. *Corros. Sci.* **2017**, *114*, 133–145.

(46) Verma, C.; Quraishi, M.; Singh, A. 5-Substituted 1H-tetrazoles as Effective Corrosion Inhibitors for Mild Steel in 1 M Hydrochloric Acid. *J. Taibah Univ. Sci.* **2016**, *10*, 718–733.

(47) Özcan, M.; Karadağ, F.; Dehri, I. Interfacial Behavior of Cysteine Between Mild Steel and Sulfuric Acid as Corrosion Inhibitor. *Acta Phys.-Chim. Sin.* **2008**, *24*, 1387–1392.

(48) Saufi, H.; Otaifah, Y. N.; Kaddi, M.; Belmaghraoui, W.; Maofari, A. A.; El Yadini, A.; El Hajjaji, S. Evaluation of the Hexanoic Anise Extract as Inhibitor for Dental Amalgam in Synthetic Saliva. *J. Mater. Environ. Sci.* **2014**, *5*, pp. 2129.

(49) Hsissou, R.; Elharfi, A.; Benassaoui, H.; Hajjaji, N.; Benhiba, F. Application of a New Trifunctional Epoxy Prepolymer, Triglycidyl Ethylene Ether of Bisphenol A, in the Coating of E24 Steel in 3.5% NaCl. *J. Chem. Technol. Metall.* **2017**, *52*, pp. 431–438.

(50) Elmsellem, H.; Aouniti, A.; Khoutoul, M.; Chetouani, A.; Hammouti, B.; Benchat, N.; Touzani, R.; Elazouzi, M. Theoretical Approach to the Corrosion Inhibition Efficiency of Some Pyrimidine Derivatives Using DFT Method of Mild Steel in HCl Solution. *J. Chem. Pharm. Res.* **2014**, *6*, pp. 1216–1224.

(51) Ebenso, E. E.; Arslan, T.; Kandemirli, F.; Caner, N.; Love, I. Quantum Chemical Studies of Some Rhodanine Azo Sulfa Drugs as Corrosion Inhibitors for Mild Steel in Acidic Medium. *Int. J. Quantum Chem.* **2010**, *110*, 1003–1018.

(52) Zarrouk, A.; Zarrok, H.; Ramli, Y.; Bouachrine, M.; Hammouti, B.; Sahibed-Dine, A.; Bentiss, F. Inhibitive Properties, Adsorption and Theoretical Study of 3,7-Dimethyl-1-(prop-2-yn-1-yl) Quinoxalin-2(1H)-one as Efficient Corrosion Inhibitor for Carbon Steel in Hydrochloric Acid Solution. *J. Mol. Liq.* **2016**, *222*, 239–252.

(53) Hsissou, R.; Abbout, S.; Seghiri, R.; Rehioui, M.; Berisha, A.; Erramli, H.; Assouag, M.; Elharfi, A. Evaluation of Corrosion Inhibition Performance of Phosphorus Polymer for Carbon Steel in [1 M] HCl: Computational Studies (DFT, MC, and MD Simulations). *J. Mater. Res. Technol.* **2020**, *9*, 2691–2703.

(54) Negm, N. N. A.; Kandile, N. G.; Badr, E. A.; Mohammed, M. A. Gravimetric and Electrochemical Evaluation of Environmentally Friendly Nonionic Corrosion Inhibitors for Carbon Steel in 1 M HCl. *Corros. Sci.* **2012**, *65*, 94–103.

(55) Solmaz, R.; Salcı, A.; Dursun, Y. A.; Kardaş, G. A comprehensive study on the adsorption, corrosion inhibition efficiency and stability of acriflavine on mild steel in 1 M HCl solution. *Colloids Surf., A* **2023**, *674*, 131908.

(56) Solomon, M. M.; Umoren, S. A.; Ritacca, A. G.; Ritacco, I.; Hu, D.; Guo, L. Tailoring poly (2-ethyl-2-oxazoline) towards effective

mitigation of chloride-induced dissolution of S235JR steel: The synergistic contributions of potassium iodide and myristyl trimethylammonium bromide. *J. Mol. Liq.* **2024**, *396*, 123935.

(57) Douche, D.; Elmsellem, H.; Anouar, E. H.; Guo, L.; Hafez, B.; Tüzün, B.; El Louzi, A.; Bougrin, K.; Karrouchi, K.; Himmi, B. Anti-corrosion Performance of 8-Hydroxyquinoline Derivatives for Mild Steel in Acidic Medium: Gravimetric, Electrochemical, DFT and Molecular Dynamics Simulation Investigations. *J. Mol. Liq.* **2020**, *308*, 113042.

(58) Sanae, L.; Elmsellem, H.; Elyoussfi, A.; Sebbar, N. K.; Essassi, E. M.; Ouzidan, Y.; Rodi, Y. K.; Dguigui, K.; El Mahi, B.; Hammouti, B. Investigation of Corrosion Inhibition of Mild Steel in 1M HCl by 3-Methyl-4-(3-methyl-isoxazol-5-yl) Isoxazol-5(2H)-one Monohydrate Using Experimental and Theoretical Approaches. *Der Pharma Chemica* **2016**, *8*, 294–303.

(59) Sebbar, N. K.; Elmsellem, H.; Boudalia, M.; Lahmidi, S.; Belleaouchou, A.; Guenbour, A.; Essassi, E. M.; Aouniti, A. An electrochemical and theoretical evaluation of new benzothiazine derivatives as a corrosion inhibitor for mild steel in HCl solutions. *J. Mater. Environ. Sci.* **2015**, *6*, pp. 3034–3044.

(60) Guadalupe, H. J.; Garcia-Ochoa, E.; Maldonado-Rivas, P.; Cruz, J.; Pandiyan, T. A Combined Electrochemical and Theoretical Study of N,N'-Bis(benzimidazole-2-yl-ethyl)-1,2-Diaminoethane as a New Corrosion Inhibitor for Carbon Steel Surface. *J. Electroanal. Chem.* **2011**, *655*, 164–172.

(61) Gadow, H.; Motawea, M.; Elabbasy, H. Investigation of Myrrh Extract as a New Corrosion Inhibitor for  $\alpha$ -Brass in 3.5% NaCl Solution Polluted by 16 ppm Sulfide. *RSC Adv.* **2017**, *7*, 29883–29898.

(62) Khadiri, A.; Saddik, R.; Bekkouché, K.; Aouniti, A.; Hammouti, B.; Benchat, N.; Bouachrine, M.; Solmaz, R. G. Gravimetric, electrochemical and quantum chemical studies of some pyridazine derivatives as corrosion inhibitors for mild steel in 1 M HCl solution. *J. Taiwan Inst. Chem. Eng.* **2016**, *58*, 552–564.

(63) Hsissou, R.; Lachhab, R.; El Magri, A.; Echihi, S.; Vanaei, H. R.; Galai, M.; Ebn Touhami, M.; Rafik, M. Synthesis characterization and highly protective efficiency of tetraglycidyl ether pentanal epoxy prepolymer as a potential corrosion inhibitor for mild steel in 1M HCl medium. *Polymers* **2022**, *14*, 3100.

(64) Hsissou, R.; Dahmani, K.; El Magri, A.; Hmada, A.; Safi, Z.; Dkhireche, N.; Galai, M.; Wazzan, N.; Berisha, A. A combined experimental and computational (DFT, RDF, MC and MD) investigation of epoxy resin as a potential corrosion inhibitor for mild steel in a 0.5 M H<sub>2</sub>SO<sub>4</sub> Environment. *Polymers* **2023**, *15*, 1967.

(65) Hsissou, R.; El Magri, A.; Ech-Chihbi, E.; Hmada, A.; Saber, L.; Berisha, A.; Dkhireche, N.; Ouzebila, D.; Rbaa, M.; Benhiba, F.; Khamliche, L.; Daoudi, M. Elaboration and investigation of formulated polymer composites as some potential anticorrosion coatings for brass surface in 3.5% NaCl solution: theoretical approaches. *Can. Metall.* **2024**, *1*–18.

(66) Ech-Chihbi, E.; Adardour, M.; Ettahiri, W.; Salim, R.; Ouakki, M.; Galai, M.; Baouid, A.; Taleb, M. Surface Interactions and Improved Corrosion Resistance of Mild Steel by Addition of New Triazolyl-benzimidazolone Derivatives in Acidic Environment. *J. Mol. Liq.* **2023**, *387*, 122652.

(67) Villamil, R.; Corio, P.; Rubim, J.; Agostinho, S. Sodium Dodecylsulfate-Benzothiazole Synergistic Effect as an Inhibitor of Processes on Copper/Chloridic Acid Interfaces. *J. Electroanal. Chem.* **2002**, *535*, 75–83.

(68) Zhang, H.; Chen, Y.; Zhang, Z. Comparative Studies of Two Benzaldehyde Thiosemicarbazone Derivatives as Corrosion Inhibitors for Mild Steel in 1.0 M HCl. *Results Phys.* **2018**, *11*, 554–563.

(69) Bousskri, A.; Anejar, A.; Salghi, R.; Jodeh, S.; Touzani, R.; Bazzi, L.; Lgaz, H. Corrosion Control of Carbon Steel in Hydrochloric Acid by New Eco-friendly Picolinium-based Ionic Liquids Derivative: Electrochemical and Synergistic Studies. *J. Mater. Environ. Sci.* **2016**, *7*, pp. 4269–4289.

(70) Roque, J. M.; Pandiyan, T.; Cruz, J.; García-Ochoa, E. DFT and Electrochemical Studies of Tris(benzimidazole-2-ylmethyl)amine as

an Efficient Corrosion Inhibitor for Carbon Steel Surface. *Corros. Sci.* **2008**, *50*, 614–624.

(71) Ech-Chihbi, E.; Salim, R.; Ouakki, M.; Koudad, M.; Guo, L.; Azam, M.; Benchat, N.; Rais, Z.; Taleb, M. Corrosion Resistance Assessment of Copper, Mild Steel, and Aluminum Alloy 2024-T3 in Acidic Solution by a Novel Imidazothiazole Derivative. *Mater. Today. Sustain* **2023**, *24*, 100524.

(72) Hjouji, M. Y.; Djedid, M.; Elmsellem, H.; Rodi, Y. K.; Ouzidan, Y.; Chahdi, F. O.; Sebbar, N. K.; Essassi, E. M.; Abdel-Rahman, I.; Hammouti, B. Corrosion Inhibition of mild steel in hydrochloric acid solution by pyrido [2, 3-b] pyrazine derivative: electrochemical and theoretical evaluation. *J. Mater. Environ. Sci.* **2016**, *7*, 4, pp. 1425–1435.

(73) Elmsellem, H.; Elyoussfi, A.; Steli, H.; Sebbar, N. K.; Essassi, E. M.; Dahmani, M.; Ouadi, Y.; Aouniti, A.; El Mahi, B.; Hammouti, B. The theobromine (chocolate) as green inhibitor of mild steel corrosion in hydrochloric acid: Electrochemical and theoretical quantum studies. *Der Pharma Chemica* **2016**, *8*, 1, pp. 248–256.

(74) Solmaz, R.; Kardaş, G.; Çulha, M.; Yazıcı, B.; Erbil, M. Investigation of Adsorption and Inhibitive Effect of 2-mercaptothiazoline on Corrosion of Mild Steel in Hydrochloric Acid Media. *Electrochim. Acta* **2008**, *53*, 5941–5952.

(75) Ellouz, M.; Elmsellem, H.; Sebbar, N. K.; Steli, H.; Al Mamari, K.; Nadeem, A.; Ouzidan, Y.; Essassi, E. M.; Abdel-Rahman, I.; Hristov, P. Anti-corrosive properties of benzothiazine derivatives on mild steel corrosion in 1M HCl solution: experimental and theoretical studies. *J. Mater. Environ. Sci.* **2016**, *7*, 7, pp. 2482–2497.

(76) Al Mamari, K.; Elmsellem, H.; Sebbar, N. K.; Elyoussfi, A.; Steli, H.; Ellouz, M.; Ouzidan, Y.; Abad, N.; Essassi, E. M.; El-Hajjaji, F. et al. Electrochemical and theoretical quantum approaches on the inhibition of mild steel corrosion in HCl using synthesized benzothiazine compound. *J. Mater. Environ. Sci.* **2016**, *7*, PP. 3286–3299.

(77) Toukal, L.; Foudia, M.; Haffar, D.; Aliouane, N.; Al-Noaimi, M.; Bellal, Y.; Elmsellem, H.; Abdel-Rahman, I. Monte Carlo simulation and electrochemical performance corrosion inhibition of benzimidazole derivative for XC48 steel in 0.5 M H<sub>2</sub>SO<sub>4</sub> and 1.0 M HCl solutions. *J. Indian Chem. Soc.* **2022**, *99*, 100634.

(78) Tanwar, A.; Pal, S. Separability of Local Reactivity Descriptors. *J. Chem. Sci.* **2005**, *117*, 497–505.

(79) Fukui, K. Role of Frontier Orbitals in Chemical Reactions. *Science* **1982**, *218*, 747–754.

(80) Sikine, M.; Elmsellem, H.; Rodi, Y. K.; Kadmi, Y.; Belghiti, M. E.; Steli, H.; Sebbar, N. K.; Essassi, E. M.; Hammouti, B.; Jazouli, A. Experimental, Monte Carlo simulation and quantum chemical analysis of 1, 5-di (prop-2-ynyl)-benzodiazepine-2, 4-dione as new corrosion inhibitor for mild steel in 1 M hydrochloric acid solution. *J. Mater. Environ. Sci.* **2017**, *8*, pp. 116–133.

(81) Lee, C.; Yang, W.; Parr, R. G. Local Softness and Chemical Reactivity in the Molecules CO, SCN<sup>−</sup>, and H<sub>2</sub>CO. *J. Mol. Struct.: Theochem* **1988**, *163*, 305–313.

(82) Cuán, A.; Galván, M.; Chattaraj, P. K. A Philicity Based Analysis of Adsorption of Small Molecules in Zeolites. *J. Chem. Sci.* **2005**, *117*, 541–548.

(83) Zouitini, A.; Rodi, Y. K.; Elmsellem, H.; Steli, H.; Chahdi, F. O.; Shariati, M. A.; Janati, A. E.; Ouzidan, Y.; Sebbar, N. K.; Essassi, E. M. Experimental and theoretical studies on inhibition of Quinoxaline derivatives against corrosion of mild steel in acidic medium. *J. Mater. Environ. Sci.* **2017**, *8*, 11, pp. 4105–4116.

(84) Kirkpatrick, S.; Gelatt, C. D.; Vecchi, M. P. Optimization By Simulated Annealing. *Science* **1983**, *220*, 671–680.

(85) Guo, L.; Zhu, S.; Zhang, S.; He, Q.; Li, W. Theoretical Studies of Three Triazole Derivatives as Corrosion Inhibitors for Mild Steel in Acidic Medium. *Corros. Sci.* **2014**, *87*, 366–375.